
SIMULATION-BASED INFERENCE OF DEVELOPMENTAL EEG MATURATION WITH THE SPECTRAL GRAPH MODEL

A PREPRINT

Danilo Bernardo^{1,†}, Xihe Xie², Parul Verma³, Jonathan Kim¹, Virginia Liu¹, Ye Wu⁴, Pew-Thian Yap⁴, Srikantan Nagarajan³, and
Ashish Raj³

¹Department of Neurology, University of California, San Francisco, San Francisco, CA, USA

²Department of Neuroscience, Weill Cornell Medicine, New York, NY, USA

³Department of Radiology, University of California, San Francisco, San Francisco, CA, USA

⁴Department of Radiology and Biomedical Research Imaging Center, University of North Carolina, Chapel Hill, NC, USA

[†]Corresponding Author: dbernardoj[at]gmail.com

May 7, 2024

ABSTRACT

The spectral content of macroscopic neural activity evolves throughout development, yet how this maturation relates to underlying brain network formation and dynamics remains unknown. To gain mechanistic insights into this process, we evaluate developmental EEG spectral changes via Bayesian model inversion of the spectral graph model (SGM), a parsimonious model of whole-brain spatio-spectral activity derived from linearized neural field models coupled by the structural connectome. Simulation-based inference was used to estimate age-varying SGM parameter posterior distributions from EEG spectra spanning the developmental period. We found this model-fitting approach accurately captures the developmental maturation of EEG spectra via a neurobiologically consistent progression of key neural parameters: long-range coupling, axonal conductance speed, and excitatory:inhibitory balance. These results suggest that spectral maturation of brain activity observed during normal development is supported by functional adaptations, specifically age-dependent tuning of localized neural dynamics and their long-range coupling within the macroscopic, structural network.

Keywords Brain modeling, Development, EEG, Spectral graph model, Bayesian inference, Simulation-based inference

1 Introduction

The human brain undergoes dynamic and complex maturational processes throughout childhood, which starts prenatally[86] and remains highly dynamic, especially from infancy to early childhood[62]. Morphological transformations of the brain across the lifespan are well established[109] and underpin well-described structural and functional network modifications occurring at various temporal and spatial scales during development[118]. However, the mechanisms linking morphological and structure-function remodeling to electrophysiological developmental changes are unknown. This gap is critical, as deviations from the typical electrophysiological maturation are associated with a spectrum of developmental disorders, including autism and epilepsy[54, 74, 84]. Here, we apply simulation-based inference (SBI)[93] in conjunction with the spectral graph model[97] to investigate structure-function dynamics that guide developmental EEG maturation.

Since Berger first reported on differences between the EEG of children and adults, the emergence of canonical brain oscillations and their expected progression has been well documented[1–3, 5, 11, 23, 31]. Principally, there is a shift in the spectral activity of wakeful states from slower frequency activity, delta (1-4 Hz) and theta (4-7Hz) activity during infancy, to faster frequencies, alpha (8-12 Hz) and beta (20-40 Hz) during adolescence and adulthood[7, 36]. There is also a well-established shift in periodic EEG spectral components, most notably the posterior dominant rhythm (PDR) gradually increases from 5-6 Hz in infancy to adult values of 8-12 Hz by adolescence[7, 35]. More recently, parameterization of aperiodic EEG spectral components has provided additional insights into age-related electrophysiological changes, such as flattening of the spectral slope seen with development[56, 66, 91, 106, 113]. Despite the critical importance of developmental electrophysiological activity as a marker to study typically developing brain networks as well as clinical applications in monitoring neurological conditions[40, 53, 70], the mechanisms underlying the spectral maturation of macroscopic brain activity remain unclear.

Mirroring M/EEG developmental studies, developmental neuroimaging studies have yielded insights into brain network development from in utero through adulthood[30, 32], and have demonstrated a tight coupling between structural and functional networks across development[8, 25, 26, 43, 98, 104]. Thus follows the intuition that maturational changes of structural and functional connectivity underlie changes in the developmental spectral content of brain oscillations[19, 31, 33, 40, 63]; however, a mechanistic understanding of this relationship has been elusive. In this regard, whole-brain simulations involving modeling of macroscopic neural activity across varying spatiotemporal scales have demonstrated promise in elucidating mechanisms of structure-function coupling[81], yet, to our knowledge, no prior studies have aimed to model the whole-brain spectral changes seen in development. As developmental EEG changes are thought to reflect the maturation of structural and functional brain networks[31, 63], spectral graph theory provides a principled foundation for the modeling of longitudinal EEG oscillatory changes as proposed in this study. Thus, we were motivated to apply the recently proposed spectral graph model (SGM), a neural mass model taking into account propagation of local neural activity across the spectral graph of the structural connectome’s Laplacian (Fig. 1A)[97]. The SGM predicts spatio-spectral frequencies of interest in electrophysiologic maturation in a parsimonious manner with a compact

set of seven key biologically-interpretable parameters (Table 1), thus making it well-suited for the aim of modeling mechanistic principles of electrophysiologic maturation that may emerge from developmental shifts in neural network properties and their underlying neuronal dynamics.

In this paper, we demonstrate the Bayesian inference of SGM parameters from a developmental EEG database to evaluate the population-based temporal evolution of SGM parameter space during the developmental period (Fig 1B-D). Estimation of brain model parameters of electrophysiological maturation from observed EEG constitutes a classic inverse problem characterized by non-uniqueness: multiple biologically plausible brain model specifications that generate similar EEG maturation trajectories. In this regard, the Bayesian approach provides a suitable framework for incorporating biophysically plausible priors as constraints and subsequent inference of SGM parameter posterior distributions[17]. We leverage recent deep learning advances in simulation-based inference that enable efficient estimation of the posterior distribution over the SGM parameters[93], and demonstrate that age-associated changes in the aperiodic and periodic components of EEG spectra are described by a neurobiologically-consistent, temporal progression of SGM parameters: long-range coupling strength (α), axonal conduction speed (S), and excitatory gain (G_{EI}). Furthermore, we validate our approach by demonstrating the prediction of age from EEG spectra with a regression model incorporating these parameters.

2 Results

2.1 Subjects

To evaluate the developmental spectral maturation of macroscopic brain activity we constructed a developmental EEG database containing EEGs from subjects ranging from 1 month to 30 years of age, containing 234 subjects (median 9 yrs, IQR 0.45 to 14 yrs). Whole-brain averaged EEG spectra are shown in Supplementary Figures 1A and 1B. The canonical emergence and increase in frequency of the posterior dominant rhythm (PDR) with advancing age is apparent in subjects older than one year, as are changes in the spectral slope of the EEG spectra.

2.2 Varying SGM Parameters Generates Spectral Shifts and Appearance of PDR

Next, we evaluated whether the spectral graph model (SGM) recapitulates spectral changes in periodic and aperiodic components of EEG spectra by systematically varying SGM parameter values to generate different spectral output realizations. Specifically, we evaluate the PDR and spectral slope, which reflects the $1/f$ distribution of aperiodic power across all frequencies[91]. Figure 2A demonstrates the emergence of the PDR with increasing values of α , mirroring the monotonic increase of PDR peak frequency that is seen with typical neurodevelopment. There is also an increase in the spectral slope with increasing values of α . Figure 2B demonstrates an increasing spectral slope in the alpha to beta frequency range with increasing values of G_{EI} . Figure 2C demonstrates a slight increase in the PDR with increasing conduction speed while the slope of the power spectra remains relatively unchanged. Figure 2D demonstrates the emergence of PDR with increasing values of G_{II} . There is also an increasing spectral slope of the alpha to beta

frequency range with increasing values of G_{II} . These changes in spectral slope generated by changes to SGM input parameters suggest that SGM is suitable for capturing changes in aperiodic $1/f$ activity seen with EEG maturation[56, 106, 113].

2.3 UMAP Analysis Demonstrates SGM Spectral Similarity to Empirical EEG Data and Parameter Space Indeterminacy

Expanding on the finding that SGM parameter variation replicates key EEG developmental spectral trajectories, we next examined the fidelity of SGM simulations to actual, empirically observed EEG spectra. Utilizing Uniform Manifold Approximation and Projection (UMAP) for dimensionality reduction of high dimensional spectra, we juxtaposed the low-dimensional latent representations of SGM simulated spectra and observed spectra. The resulting UMAP embeddings are shown in Figures 2E-F and Supplementary Figure 2, with total 196,000 SGM realizations displayed. Supplementary Figure 2 demonstrates an overlap between the simulated SGM and observed EEG spectral embeddings, indicating that SGM parameter variation replicates real-world EEG spectral features observed across development. Figures 2F and 2G, wherein UMAP embedding color is determined by respective spectral PDR and aperiodic exponent, demonstrate regions with homogeneous PDR frequency or aperiodic exponent. This indicates model indeterminacy or regimes in SGM parameter space that yield similar spectral features.

2.4 Non-specificity of Structural Connectome on Spectral Shifts and Appearance of PDR

We utilized the template HCP structural connectome[44] in these parameter variation analyses and subsequent analyses due to the lack of age-specific structural connectomes across the broad pediatric age ranges and fine temporal resolutions (weeks) required for our study. To assess the significance of excluding age-dependent connectomes, we contrasted SGM realizations derived from the structural connectivity at two developmental extremes—neonatal and adult. We evaluated the effect of different structural connectivity in the neonatal versus adult structural connectomes on SGM spectral realizations at both strong and weak long-range coupling (α) regimes. There were subtle region-specific spectral differences between adults and neonates, reflecting variations in anatomical structural connectivity. However, a comparison of the neonatal and adult SGM spectral distributions with Jensen-Shannon divergence (a bounded symmetrization of the Kullback–Leibler divergence between 0 to 1) demonstrated low divergences less than $1e-2$ across all brain regions (Figure 3). Importantly, the utilization of either neonatal or adult structural connectomes did not substantially alter aperiodic $1/f$ activity and PDR. In contrast, the transition from weak to strong long-range coupling with neurodevelopment markedly influences both. This finding suggests that the specificity of structural connectomes in $1/f$ activity and PDR generation is limited, corroborating recent evidence from the developing Human Connectome Project (dHCP) indicating that core structural connectome components are established in utero and stable postnatally[110]. Therefore, although the utilization of a static structural connectome does not encompass all structural network changes affecting spectral maturation, it nonetheless offers a foundation to understand how spectral

maturation may emerge from age-dependent tuning of localized neuronal dynamics and their long-range coupling within a conserved structural network.

2.5 SBI Sensitivity Analyses, Posterior Diagnostics, and Simulation-based Calibration

To elucidate key parameters driving EEG spectral development, we utilized a Bayesian approach employing simulation-based inference (SBI) to identify approximate posterior distributions of SGM parameters that best align with synthetic or empirical EEG spectra. We evaluated three recent SBI methods: Neural Ratio Estimation (NRE)[95], Automatic Posterior Transformation also known as Neural Posterior Estimation (NPE)[82], and the recently introduced truncated sequential NPE (TSNPE), which more robustly handles posterior estimation at the boundaries of the specified prior range[111]. In order to assess the accuracy and robustness of the SBI-SGM inference framework, we conducted parameter recovery analyses and simulation-based calibration (SBC) with synthetic data as outlined in Supporting Information 1.

NRE, NPE, and TSNPE demonstrated differential performance across parameter recovery and SBC, with NPE and TSNPE generally outperforming NRE (Supplementary Figures 3-10). While NPE demonstrates robust parameter recovery, it tends to produce poorly calibrated posterior distributions (Supplementary Figure 11) and is prone to posterior leakage at the parameter bounds (Supplementary Figure 12). In contrast, TSNPE has well-calibrated posteriors relative to NPE; however, its scalability is limited under conditions of extensive simulation requirements and large datasets. We discuss potential sources of the differential performance across SBI methods further in Supporting Information 2. Given the general preference for conservative over overconfident posterior estimates—the latter potentially leading to erroneous scientific conclusions[117]—we utilize TSNPE in subsequent application of SBI-SGM to empirical data given its improved calibration results compared to NPE.

2.6 SBI of SGM Parameters Recapitulates Observed EEG Spectral Features

Having assessed the robustness of the inference procedure, we next performed a posterior predictive check on empirical data, specifically simulating spectra under the fitted SGM and then comparing these to the observed data. Figure 4 (red traces) demonstrates examples of output SGM spectra realized from mean values of the SGM parameter posterior distribution inferred with TSNPE that resemble the input empirical EEG spectra (black traces). These examples recapitulate periodic and aperiodic components of the empiric EEG spectra, confirming that SBI with SGM captures relevant spectral features of observed EEG data, including periodic and aperiodic features such as PDR and spectral slope. The corresponding posterior distributions for each respective EEG spectrum SGM model fit with TSNPE are shown in Figure 4 (right panels), with higher probabilities assigned to SGM parameter sets that generate realizations consistent with the observed data and lower probabilities to inconsistent parameter sets. NPE and TSNPE had similar PDI profiles for empirical data, with both demonstrating excitatory and inhibitory time constants as having the least dispersion and conduction speed as having highest dispersion (Supplementary Figure 11).

2.7 Simulation-based Inference of SGM Parameters Shows Age-Related Increases in Global Coupling, Neural Conduction Speed, and Excitatory and Inhibitory Gains

Next, we aimed to ascertain if age-dependent trajectories in the SGM parameter posterior distributions, inferred from real EEG data, would align with established age-dependent changes in their biological counterparts. These developmental trends include well-known increases in functional long-range connectivity and coupling strength[107, 116], acceleration of axonal conduction speed [69], and shift towards reduced excitatory:inhibitory balance with aging[58, 75, 89]. To achieve this, we allowed the SBI-SGM inference to operate within physiologically plausible prior bounds, but no other enforced constraints thereby allowing model flexibility within a broad parameter space. This approach allowed us to evaluate the natural evolution of SGM parameter posterior distributions across the developmental time frame.

We inferred multivariate SGM posteriors for each subject with TSNPE (Supplementary Figures 14 and 15), then retrieved the posterior means from the probability density function for each respective SGM parameter posterior distribution. Figure 5 demonstrates plots of the subsequent mean SGM parameter values versus the respective age for each subject. Notably, there was a significant positive association between age and long-range coupling α (Pearson correlation coefficient $r = 0.615$, $p < 1e-3$). Considering that α reflects functional long-range coupling of neural dynamics unfolding over a seconds-scale timespan[125], the protracted increase in PDR occurring over years during neurodevelopment suggests a gradual enhancement in the baseline tone of long-range functional coupling within the connectome. Biologically, this may be mediated by the strengthening of long-range excitatory and GABAergic coupling that occurs during neurodevelopment[107, 116].

In addition, our results indicate an age-related increase in axonal conduction speed S ($r = 0.722$, $p < 1e-3$), consistent with the known maturation of white matter pathways, which also importantly impacts long-range coupling[69]. This finding is congruent with the established maturation of white matter myelination and axon diameter, which are the primary determinants of conduction speed[29, 51].

Furthermore, we demonstrate a reduction in E:I gain ratio (G_{EI} : $r = -0.489$, $p < 1e-3$; G_{II} : $r = 0.388$, $p < 1e-3$), mirroring animal model studies that have reported a developmental decrease in the E:I ratio, putatively driven by an increase in GABAergic tone[38, 102]. Also, recent human studies have investigated TMS to measure and affect the E:I ratio[75, 89], and the finding of reduced E-I during development aligns with TMS study findings that older individuals tended towards greater intrinsic inhibitor tone[58].

Lastly, τ_e and τ_i demonstrated negative associations with age with $r = -0.363$ and $r = -0.641$ (both with $p < 0.001$), while there were no associations between age and τ_G (Supplementary Figure 16). These reductions in τ_e and τ_i are potentially congruent with rodent and primate studies which have reported a general quickening of GABAergic and glutamatergic synaptic time constants over the developmental period[6, 10, 16, 21, 50]. However, regression diagnostics with scale-location plots (Supplementary Figure 17) for τ_e and τ_i indicated heteroskedasticity confirmed by Breusch-Pagan tests with χ^2 of 5.560 and 14.13 with corresponding p -values of 0.0179 and 1.71e-3, respectively. The

presence of significant heteroskedasticity limits the reliability and validity of the τ_e and τ_i findings. The other SGM parameters did not exhibit significant heteroskedasticity.

2.8 Prediction of Age and PDR with Data-Driven Inference of SGM Parameters

For further validation of the age-dependent trajectories of the inferred SGM parameter posterior distributions, we next asked whether the inferred SGM parameters could predict subject ages from the input EEG spectra. Employing polynomial regression, we modeled the relationship between SGM parameters that were demonstrated in the preceding analysis to have a robust linear relationship with age (α , S , G_{EI} , G_{II}) with log age. We evaluated the predictive capacity of the regression model on observed versus predicted age using a cross-validation approach and compared performance to a polynomial regression model fit on periodic and aperiodic parameters obtained with the *fitting oscillations & one over f* (FOOOF) methodology[91]. We evaluated for heteroskedasticity with the Breusch-Pagan test and the SBI-SGM regression model did not exhibit heteroskedasticity (Supplementary Figure 18). The adjusted coefficient of determination (R^2) for observed versus predicted age was 0.534 (Figure 6a, left panel), consistent with good agreement between SBI-SGM regression model predicted age and observed age. This demonstrates improved performance over the FOOOF regression model, which had (R^2) of 0.534 (Figure 6a, right panel). We then evaluated whether SBI of SGM parameters would correspond with spectral changes in the PDR over time. We modeled this relationship using polynomial regression and found an adjusted R^2 of 0.217 for observed versus predicted PDR (Figure 6b), suggesting that the evolution of SGM features during development only partially accounts for the observed variance in periodic EEG spectral features. In comparison, the FOOOF model fit on aperiodic $1/f$ exponent and intercept achieved R^2 of 0.55, suggesting that aperiodic $1/f$ features evolution during aging are predictive of PDR frequency. Prior literature in predicting age from EEG has reported R^2 values ranging up to 0.61 for datasets including pediatric subjects with best results achieved utilizing machine learning approaches [112]. Engemann et al. reported deep learning and feature-engineering models had R^2 values of 0.61 and 0.33, respectively, on the normal subgroup of the Temple University Hospital Abnormal (TUAB) EEG dataset (N=1385, mean age: 48.6 yrs with standard deviation 17.9 years)[112]. Given that TUAB predominantly consists of adult subjects with 43 subjects between 10-20 yrs and only three subjects in the 0-10 yrs, direct comparison with our findings, which focus on the developmental age demographic, is limited. In contrast to DL approaches or feature engineering approach utilized by Engemann et al. which utilized at least 30 features, the SGM approach demonstrates comparable performance while utilizing a minimal, biophysically-principled feature set with only 7 parameters, thus providing model interpretability and insight into the underlying brain dynamics correlated with aging and development.

3 Discussion

3.1 Overview

In this study, we utilize simulation-based inference with the spectral graph model (SBI-SGM) to model EEG spectral maturation and infer population-based trajectories of SGM parameters relevant to brain development, such as long-range coupling and excitatory-to-inhibitory (E:I) gains. We demonstrate that the temporal progression of SGM parameters coheres with their expected developmental evolution. To our knowledge, this is the first demonstration that the maturation of brain spectra across developmental stages can be accurately modeled within an analytical framework, guided by the neurobiologically consistent evolution of model parameters.

3.2 Neurobiologically Consistent Developmental Evolution of Inferred SGM Parameters

The maturation of long-range projection fibers, marked by myelination and axonal diameter growth, are considered crucial in promoting structure: function coupling thereby mediating the evolution of diverse functional network configurations and their underlying brain rhythms, such as the posterior dominant rhythm (PDR)[28, 31, 34, 47, 55, 87]. However, recent evidence indicates that the connectome’s structural core is already present and remarkably stable in infancy and early childhood. This suggests the presence of additional mechanisms contributing to the postnatal refinement of functional networks.

In exploring these mechanisms with SGM-SBI, we identified that an increase in long-range coupling (α) during development captured the canonical age-dependent increase in the PDR. While PDR and other oscillations can be generated via neural mass models modeling cortical columns or the thalamocortical system [9, 12, 27, 39, 46], to our knowledge how certain brain oscillations such as PDR may emerge and evolve at expected time points in the lifespan has not been previously specified with a mechanistic whole-brain model. Our findings suggest that PDR evolution is partially driven by age-dependent alterations in network dynamics underpinned by the gradual strengthening of long-range functional coupling over the structural connectome[116]. Also, our results recapitulated the known increase in axonal conduction speed with age, which facilitates transmission efficiency and thus functional organization of long-range neural networks[42, 69]

Finally, we demonstrated that E:I balance demonstrated a reduction with age, congruent with the established reduction of E:I balance that occurs with development, thought to be primarily mediated by the maturation of GABAergic circuitry[14, 15, 52]. Fine-tuning of E:I balance has been demonstrated across different brain regions and disruptions to E:I balance have been implicated in animal models of autism and other disorders of disrupted neurodevelopment[38, 49, 54, 84]. We assumed uniform levels of excitation and inhibition, respectively, occurring at a mesoscopic level throughout the whole brain network model of the SGM. While this is a simplified treatment of E:I balance, we recognize that excitation and inhibition are, in fact, multidimensional entities, occurring across multiple network scales, varying time periods, and mediated by diverse excitatory and inhibitory cell types and synaptic mechanisms[84]. Nonetheless,

SGM provides an analytical foothold in the challenge of understanding E:I balance by relating changes to configurations of excitatory or inhibitory gains to predicted brain spectral activity[97].

3.3 Spectral Graph Model Applied to Investigating Developmental Network Changes

Spectral graph theory, and in particular one of its central tenets the graph Laplacian operator, has broad applicability and effectiveness across multiple domains in network science[18], thus has emerged as a powerful tool for understanding structure–function relationships in neuroscience. Indeed, eigenmodes of the brain network Laplacian, as introduced by Abdelnour et al. and others, have been used to predict canonical functional networks from underlying structural networks[20, 45, 48]. These models are intimately related to walks on graphs, and higher-order walks on graphs have also been quite successful; typically, these methods involve a series expansion of the graph adjacency or Laplacian matrices[60, 72]. It is now known that the series expansion and eigenmode approaches yield highly similar mappings between functional and structural network[61, 90, 100]. In the latter, eigenmodes of the adjacency or Laplacian matrix are typically employed, and only a few eigenmodes are usually sufficient to reproduce empirical functional connectivity[57, 61, 71, 83, 92, 101, 108]. While the above eigenmode-based models have demonstrated the ability to capture steady-state, stationary characteristics of real brain activity, they are limited to modeling passive spread without oscillatory behavior. Capturing the rich repertoire displayed by EEG recordings would require a full accounting of axonal propagation delays as well as local neural population dynamics within graph models. Band-specific MEG resting-state networks were successfully modeled with a combination of delayed neural mass models and eigenmodes of the structural network[85], suggesting delayed interactions in a brain’s network give rise to functional patterns constrained by structural eigenmodes. The SGM further develops this concept by demonstrating the prediction of spatial and spectral features of neural oscillatory activity providing a parsimonious representation of the spatio-spectral distribution of brain oscillations[97]. Despite the inherent nonlinearities present in the brain, particularly at microscopic and mesoscopic scales, a recent study comparing linear and nonlinear approaches of modeling macroscopic intracranial EEG and fMRI neurophysiologic activity demonstrated that linear models unexpectedly performed more accurately than nonlinear models, thus suggesting advantages to the linear modeling approach in their relative interpretability compared to nonlinear models[123]. However, it is crucial to recognize that the inherent nonlinearities and complexities of brain network dynamics may be more faithfully represented through nonlinear modeling[65]. Thus, the advantageous interpretability and computational tractability of linear models such as the SGM should be seen as a complement to, rather than a replacement for, nonlinear methods.

3.4 Comparison to Prior Works

The SGM provides a robust framework for modeling age-related changes in aperiodic and periodic spectral components, attributing the functional maturation of brain activity to age-dependent modulation and interplay of localized and long-range network dynamics. Here, we contrast our study to prior approaches to modeling whole brain activity. While there have been numerous large-scale neural network or macroscopic brain models of alpha frequency rhythms

(PDR) proposed, these have been limited to modeling alpha activity in relatively more temporally constrained brain states, such as during anesthesia[9, 27, 37, 39]. While these approaches successfully captured oscillatory brain activity[9, 27, 39], they did not aim to simultaneously model aperiodic brain activity. Conversely, Bedard and Destexhe developed a framework for the genesis of aperiodic brain activity; however, this framework did not capture periodic oscillations[24]. Notably, Hashemi et al. utilized Bayesian inference techniques, including Monte Carlo Markov Chain methods, to effectively fit a thalamocortical neural mass model to EEG data in humans undergoing anesthesia, demonstrating effective capture of key spectral peaks in delta and alpha frequencies, as well as aperiodic components, in observed data[77]. Few studies have appeared to utilize a regional or whole-brain network approach to seek to explain spectral periodic and aperiodic activity. Notably, an approach utilizing the Kuramoto model with a whole brain connectome suggested mechanistic underpinnings of alpha and beta activities arising from cross-regional synchronization; however, de-emphasized the accuracy of their simulation at capturing realistic brain activity[46]. Our approach aligns with the perspective that the basis of functional brain activity arises from network synchronization, and moreover, offers a mechanistic framework for how EEG spectral maturation is directly linked to age-dependent tuning of this synchronization.

3.5 Stability of Findings

The stability or robustness of our findings hinge on several aspects: data characteristics and degree of model misspecification; SBI components such as prior specification and posterior approximator hyperparameterization[119]; and the stability of the SGM itself. Regarding dataset characteristics, the experimental data distribution, noise levels, and alignment (or misalignment) of the model with the data-generating process may affect SBI robustness[126]. EEG data demonstrates substantial variability across the developmental timeline. Thus, depending on the age group of interest, a more targeted analysis within narrower developmental windows may yield more robust inferences due to decreased variability and the option to use age-specific priors. Concerning stability considerations related to the SBI, our evaluations utilizing synthetic reference data demonstrated that stability and accuracy of posterior distributions, given a priori knowledge of the true solution, depended on NPE hyperparameterization, such as the simulation budget utilized. In addition, one may consider approaches to improve SBI stability and reliability, including ensembling and post-hoc calibration methods[103]. Further work involving generalization studies on larger datasets is required to effectively evaluate the stability of the SBI-SGM framework.

Regarding numerical stability of the SGM model itself, Verma et al. applied root locus analysis to delineate the bounds of SGM parameters that give rise to dynamical behaviors, including damped oscillations, limit cycles, or unstable oscillations[125]. Our SBI findings for excitatory and inhibitory time constants and alpha were within ranges that promote stable oscillatory activity. In contrast, excitatory:inhibitory gains were consequently inferred to be above boundaries that ensure stable oscillations, suggesting a potential for instability. These parameters exhibited increased posterior dispersion and variance in identifiability, which could reflect the unstable regime in SGM parameter space leading to greater unpredictability in SGM output. However, our empirical data encompassed subjects wherein

oscillatory activity demonstrated fluctuations and instability over the monitoring duration, was intermixed within prominent $1/f$ activity, or was absent in the case of younger infants. The ability of the SGM to account for such diverse neural dynamics promotes robustness in the SBI-SGM framework, particularly in accommodating the unpredictability and instabilities of whole-brain network activity.

3.6 Limitations

In this study, a notable limitation arises from the non-utilization of age-specific structural connectomes from birth to adulthood; rather, analysis was performed using a standardized adult connectome. This constraint is primarily due to scarcity of available age-specific structural connectome datasets for the 0 to 24 month old age range with fine-grained age resolution. Consequently, our analysis does not account for potential changes in the structural connectome that may contribute to spectral maturation. Recent evidence suggests that the structural connectome forms in utero[67, 76]. Notably, in a recent study in premature neonates who received serial neuroimaging, Ciarrusta et al. demonstrated that the core components of the structural connectome develop in utero and are relatively stable postnatally, [110]. In addition, the functional connectome fingerprint is not only established, but also demonstrates stability during early brain development in infants[114]. Despite the limitations arising from the use of a static structural connectome in our analysis, maintaining a stable structural network over the developmental age range aligns with recent findings on the stability of a core structural network and provides insight into how functional changes arise upon a consistent structural framework.

Additionally, we acknowledge a potential limitation in our analysis arising from relatively unrestricted parameter exploration, constrained only by bounds on SGM time constants and propagation parameters. During SBI and within the SGM, we did not enforce neurobiological constraints, thus the inferred SGM parameter realizations may not necessarily align with naturally observed relationships in the parameters. Notably, Hashemi et al. utilized neurobiological constraints enforced during spectral fitting, such as differential response function characteristics for excitatory and inhibitory synapses with excitatory response function having longer rise and decay times than inhibitory synapses[77]. Within the proposed SBI-SGM framework, we purposefully do not directly enforce neurobiological constraints with the aim of capturing a parsimonious model of brain spectral evolution over development. Nevertheless, introducing such constraints would enable further alignment of SBI of brain and neural models with naturally occurring observed constraints.

Also, given that our empirical data constitutes an average EEG spectrum across channels, it may be argued that fitting such a signal does not require a spatially resolved model like the SGM. In fact, one could fit the empirical spectrum to a single lumped neural mass model[12]. More detailed models are also available[96]. Such models would incorporate local dynamic properties like E:I gain and local circuit time constants. However, they would be unable to probe the specific maturation behavior of interest seen developmentally - i.e., of axonal conductance speed and inter-regional coupling. Another benefit of a spatially-resolved model such as the SGM is that in future studies with denser EEG configurations or scalp MEG, it would be possible to perform reliable source reconstruction, which will in turn enable

the interrogation of the spatial gradients of empirical electrophysiology, in addition to their spectral content. This would, for instance, allow us to explore the ability of fitted model to reproduce the spatial dominance of alpha rhythm, analogous to that recently demonstrated in adults[97, 108].

3.7 Implications and Future Directions

The ability of SBI capture age-dependent changes in SGM parameters from empirical EEG data suggests broader applicability. For instance, in epileptogenesis, elucidating the time-dependent slow dynamics of long-range coupling and excitatory:inhibitory balance may provide insights into pathologic neurophysiological shifts that engender the development of epilepsy, whereas identifying rapid changes in these parameters could elucidate dynamics of pre-ictal and ictal states. Similarly, deviation of these parameters from typical trajectories could be used to investigate spectral differences that arise in autism and other neurodevelopmental disorders. Lastly, recent work by Lavanga et al. has utilized SBI in conjunction with whole brain modeling to understand structure-function relationship underlying cognitive decline in aging[122]. Similarly, the SGM, which has been recently used to model abnormal neural oscillations and their cellular correlates in patients with Alzheimer’s Disease[115], in conjunction with SBI offers an analytical framework to further investigate mechanisms underlying cognitive decline. The potential for SBI in conjunction with the SGM to provide novel mechanistic insights into both normal neurodevelopment and conditions with disrupted neurodevelopment, such as autism and epilepsy, will be evaluated in future work.

3.8 Conclusions

While the critical trajectories of morphological and structural connectivity remodeling during development are well-established, the structure-function relationship remains to be clarified. Our findings suggest that the evolving structure-function interplay influences canonical features of brain spectral maturation, including the evolution of PDR and $1/f$ aperiodic activity. This interplay is inextricably linked to changes in brain morphology and structural networks, yet understanding the precise mechanisms underlying this connection warrants additional investigation.

4 Methods

4.1 Spectral Graph Model

The SGM is a linear model capable of simulating spatial and spectral patterns of macroscopic neural activity. In this hierarchical model of the brain’s structure-to-function relationship, the macroscopic functional activity emerging from mesoscopic neural activity is summarized by a minimal set of global macroscopic parameters in a closed-form Fourier domain formulation. The simulated broadband spectrum and spatial patterns emerge from the information-rich contents of the brain’s structural graph Laplacian. The key concepts of the macroscopic model will be highlighted here, while the detailed derivations are illustrated in the original publications[97, 108].

4.1.1 Complex Graph Laplacian

For a brain’s white matter diffusion-derived structural network, its normalized graph Laplacian matrix characterizes the most probable paths a signal may take in a network. Here, we define the brain’s structural connectivity matrix as $\mathbf{C} = c_{j,k}$, consisting of connection strengths between any brain regions j and k . To incorporate the time delays caused by white matter streamline distances between brain regions, we utilize the properties of delay-induced phases in the Fourier domain and introduce a complex-valued connectivity matrix $\mathbf{C}^*(\omega) = c_{j,k} \exp(-j\omega\tau_{j,k}^v)$. Where delays $\tau_{j,k}^v$ is computed from the pairwise region distances divided by a constant velocity v . This complex connectivity matrix not only incorporates distance-induced delays between nodes ($\tau_{j,k}^v$) into our network but also allows us to estimate network properties given a frequency of oscillation (ω). Therefore, a degree normalized complex connectivity matrix at some frequency ω is defined as:

$$\mathbf{C}(\omega) = \text{diag}\left(\frac{1}{\mathbf{deg}}\right)\mathbf{C}^*(\omega) \quad (1)$$

Where the degree vector \mathbf{deg} is defined as $\mathbf{deg}_k = \sum_j c_{j,k}$. The SGM propagates signals via the eigenmodes of the network’s Laplacian matrix, and a normalized Laplacian \mathcal{L} of $\mathbf{C}(\omega)$ is defined as:

$$\mathcal{L}(\omega) = \mathbf{I} - \alpha\mathbf{C}(\omega) \quad (2)$$

Where \mathbf{I} is the identity matrix and α is a global coupling constant parameter that weights the network connections.

4.1.2 The Macroscopic Model

The macroscopic model relies on the assumption that signal transmission between macroscopic brain regions is linear, and the changes in the signal’s spectral contents can be summarized by linear filters. In the SGM, this macroscopic linear filter is a Gamma-shaped function $F(\omega) = \frac{\frac{1}{\tau^2}}{(j\omega + \frac{1}{\tau})^2}$. These linear filters in combination with the complex valued network Laplacian dictates the spectral and spatial spreading of signals from mesoscopic neuron assemblies:

$$\mathbf{X}(\omega) = (j\omega\mathbf{I} + \frac{1}{\tau_G}F(\omega)\mathcal{L}(\omega))^{-1}\mathbf{H}_{local}(\omega)\mathbf{P}(\omega) \quad (3)$$

In steady-state conditions, we assume the brain has uncorrelated Gaussian noise, therefore the driving function $\mathbf{P}(\omega) = \mathbf{I}$, where \mathbf{I} is a vector of ones. The network level time constant τ_G parameterizes the macroscopic properties of the brain's structural network and region wise activity $\mathbf{H}_{local}(\omega)$ is transferred throughout the network via the characteristic paths set by the Laplacian $\mathcal{L}(\omega)$. The characteristic paths are computed by the eigendecomposition of $\mathcal{L}(\omega)$:

$$\mathcal{L}(\omega) = \mathbf{U}(\omega)\mathbf{\Lambda}(\omega)\mathbf{U}^H(\omega) \quad (4)$$

Where $\mathbf{\Lambda}(\omega) = \text{diag}([\lambda_1(\omega), \dots, \lambda_N(\omega)])$ is a diagonal matrix consisting of the eigen values of $\mathcal{L}(\omega)$. By incorporating the eigen modes $\mathbf{U}(\omega)$ into (3), we can show that the macroscopic frequency profile $\mathbf{X}(\omega)$ is:

$$\mathbf{X}(\omega) = \sum_i \frac{\mathbf{u}_i(\omega)\mathbf{u}_i^H(\omega)}{j\omega + \frac{1}{\tau_G}\lambda_i F(\omega)}\mathbf{H}_{local}(\omega)\mathbf{P}(\omega) \quad (5)$$

An overview of the SGM is shown in Figure 1A.

4.2 UMAP of SGM simulations

To understand the SGM parameter space and evaluate the ability of the SGM to capture developmental EEG spectral shifts we utilized UMAP (Uniform Manifold Approximation and Projection) for dimension reduction of spectra and visualization of SGM simulated spectra and observed EEG spectra, using hyperparameters number of neighbors of 60 and minimum distance of 0.1[78]. This generates a low dimensional embedding of potential simulated SGM spectra and observed EEG spectra on which spectra that self-similar will cluster. Similarity between SGM spectra and observed spectra will manifest with overlapping clusters of these respective groups and conversely dissimilarity between the two groups will manifest as clusters with minimal or no overlap. To allow a balanced input to UMAP that is representative of the canonical EEG power bands, we provide as input to UMAP individual frequency binned power from 0.5 Hz to 12 Hz in 0.5 Hz bins, average power in the high alpha (12-20 Hz), beta (20-40 Hz), and gamma (40-55 Hz).

4.3 Subject EEG and Standardized Structural Connectome

A total of 234 subjects aged between 1 month to 30 years were included in this study. We utilized publicly available neonatal and infant EEG datasets with age range 1 month to 1 year of age[80]. We also utilized a publicly available database of EEGs containing ages 5 to 18 years of age[64]. Additional EEG data were used from patients with normal EEG between the ages of 1 day to 5 years of age were retrospectively identified from the University of California San Francisco (UCSF) Epilepsy Monitoring Unit EEG Database or the UCSF Benioff Children's Hospital Neuro-Intensive

Care Nursery database and selected for analyses with the following inclusion criteria: (1) Normal EEG at time of study and (2) No known history of seizures, stroke, or other known neurological condition at the time of study. All study procedures were approved by the institutional review board at UCSF. All EEG used were standard 10-20 system with averaged reference montage with total 19 channels. For calculation of EEG spectra we calculate the power spectral density (PSD) using Welch’s method in 100 frequency bins between 0 to 50 Hz, which is less than half the sampling rate for all EEGs. This pre-processing was performed with the Python MNE package[41]. To constrain dimensionality, we utilize the global mean across all channels for both observed and simulated spectra.

For SGM spectral realizations used in the main analysis, we utilized the adult template structural connectome obtained from the MGH-USC Human Connectome Project (HCP) database [44]. We compared SGM realizations derived from the adult HCP connectome to those derived from a template neonatal connectome. The template neonate connectome was derived from 20 full-term neonates from the developing Human Connectome Project (dHCP)[68].

4.4 Simulation Based Inference of SGM Parameters

A challenge central to neural modeling is the statistical inference of simulation model parameters, with respect to observable data, which in Bayesian inference, can arise due to computational intractability of the posterior distribution for high dimensional systems or analytical intractability of the likelihood function[88]. In this regard, recent advances in simulation-based inference leveraging deep learning advances to approximate the posterior distributions for respective simulation parameters have shown promise in application to single-neuron mechanistic models[93], and more broadly have seen increasing utility in diverse scientific fields including particle physics and astrophysics[88]. The potential of simulation-based inference to model high-dimensional whole-brain dynamics has recently been leveraged in modeling epilepsy and in healthy brain aging[120, 122].

Modeling neural data is hindered by the inaccessibility of the ground truth set of biophysical parameters across the microscopic to macroscopic continuum that determine the human brain’s structural and functional state. Furthermore, even if these parameters were available, the likelihood function becomes computationally intractable in the face of high-dimensional complexity characteristic of neural data. Moreover, traditional MCMC methods used for Bayesian inference, while powerful are computationally inefficient, particularly when applied to high-dimensional neural modeling and may have convergence issues[121]. In this context, recent developments in probabilistic models in machine learning (ML) have led to methodological advances in simulation-based inference (SBI), including deep-learning based compact representation of high-dimensional data, active learning methods to simulate at parameters θ that have higher likelihood of increasing knowledge the most, and amortization of probability density estimation[88]. In our approach, we evaluated three recent SBI techniques: Neural Ratio Estimation (NRE)[95], Neural Posterior Estimation (NPE)[82], and Truncated Sequential Neural Posterior Estimation (TSNPE)[111]. In NRE, a neural network classifier is trained to approximate the likelihood-to-marginal ratio[95]. In NPE, which is also known as automatic posterior transformation (APT) and sequential NPE (SNPE) when utilized in multi-round inference contexts, the generative model is run sequentially across different sets of parameters generating model behavior on which a deep neural network can be trained to output a

posterior distribution over the input model parameters[82]. This approach, which circumvents direct computation of the likelihood function, has recently been effectively applied in the domain of functional to structural brain modeling in the context of healthy brain aging[122]. We also compare standard NPE to the recently introduced truncated NPE (TSNPE), which more robustly handles posterior estimation near the margins of the specified prior range compared to NPE[111]. While we focus on recent SBI methods here, we acknowledge that there are alternative robust methods for parameter estimation. A prominent Bayesian inference approach is the Hamiltonian Monte Carlo (HMC) algorithm, which offers superior convergence and robustness in handling high-dimensional spaces and models with highly correlated parameters relative to traditional MCMC methods[4]. Whereas in SBI, neither the model nor summary statistics features are required to be differentiable, HMC necessitates model differentiability, as it employs gradient calculations of the log posterior with respect to the model’s parameters to compute the Hamiltonian dynamics, facilitating efficient exploration of the posterior distribution. A compelling demonstration of these gradient-based HMC methods in combination was demonstrated by Hashemi et al. for the inversion of a differentiable whole-brain model to model subject-specific epileptogenicity[94]. The SGM is differentiable; however, caution and further investigation are needed to evaluate the stability of eigendecomposition gradients due to parameter degeneracy and the use of non-Hermitian matrices in the SGM.

Given the observed EEG spectra y , the respective SGM parameter posterior distribution $p(\theta | y)$ was determined by NRE, NPE, or TSNPE utilizing the *sbi* Python package[82, 99]. In this approach, SGM is evaluated sequentially across specified parameter value ranges generating SGM spectral output realizations on which the neural density estimator is trained to approximate the posterior distribution over the input model parameters (Figure 1B). Prior knowledge is parameterized in the SGM as the range of admissible values for θ based on biophysically plausible values following Raj et al.[97]. SGM parameters and their respective bounds used for SBI are listed in Table 1. We evaluated varying simulation budget sizes up to $1E6$ simulations to train the neural density estimator for NRE and NPE. For TSNPE, we evaluated varying budget sizes up to 2000 simulations at two or three rounds of sequential inference with proposal truncation. We utilized summary statistics of SGM power spectral density (PSD) output, the first periodic and aperiodic components (Supplementary Figure 1C) which succinctly parameterizes physiologically and developmentally pertinent EEG spectral features[91, 106], and binned PSD as utilized by Rodrigues et al. for neural mass model (NMM) inversion with Hierarchical Neural Posterior Estimation[105]. The resulting inferred posterior distributions $p(\theta | y)$ contain high values for parameters θ that are consistent with the empirical data y and are asymptotic to zero for θ inconsistent with y (Figure 1C, right panel). 10000 samples (i.e., consistent SGM parameter sets) per subject were drawn from the posterior $p(\theta | y)$ to determine the multivariate posterior distribution. The distributions of $p(\theta | y)$ over y observed across different ages were used to evaluate longitudinal changes of θ and for incorporation into subsequent regression models.

4.5 Bayesian Sensitivity Analysis

Bayesian identifiability and sensitivity analyses, which assess the Bayesian joint distribution and inference process, are utilized to identify pathology in the inference approach and to characterize the performance of the inference

procedure[73]. The Bayesian joint distribution is determined by the model configuration space and the prior distribution: $\pi(y, \theta) = \pi(y|\theta)\pi(\theta)$; and is conditioned upon on an observation, \tilde{y} , to obtain the posterior distribution[73]. We evaluate the posterior shrinkage[73], defined as $s = 1 - \frac{\sigma_{\text{post}}^2}{\sigma_{\text{prior}}^2}$. If the posterior closely resembles the prior without significant shrinkage, it indicates structural non-identifiability, as the data does not inform our understanding of these parameters. Conversely, when the posterior is influenced by the data (evidenced by shrinkage) but demonstrates a strong statistical interdependence among parameters, this indicates either structural or practical non-identifiability, characterized by an inability to uniquely determine individual parameters due to their interrelated nature in the model[13]. In addition, the posterior z -score may be used to assess how accurately the posterior recovers ground truth parameters. We evaluate the posterior z -score[73], defined as: $\mathbf{z} = \left| \frac{\mu_{\text{post}} - \tilde{\theta}}{\sigma_{\text{post}}} \right|$ where μ_{post} is the posterior mean, σ_{post} is the posterior standard deviation, and z quantifies how accurately the posterior mean approximates the true parameter.

4.6 Simulation-based Calibration of SBI-SGM

Simulation-Based Calibration (SBC) is used to validate the precision of uncertainties within the Bayesian framework by assessing whether the variance in the posterior distribution, which represents uncertainty in model parameters, is accurately calibrated[79]. SBC involves generating multiple observational datasets from a range of parameters drawn from the prior distribution, then for each dataset, a posterior distribution is computed using SBI. The subsequent posterior calibration is deemed accurate if the ranks of the original parameters, when evaluated within their corresponding posterior distributions, collectively exhibit a uniform distribution. The uniformity of the resulting SBC ranks is then visually assessed by comparing their empirical cumulative density function to that of an ideal uniform distribution, ensuring the reliability of the model’s uncertainty estimations. This uniformity of the normalized rank statistics aligns with a necessary, though not sufficient, condition for the estimated posterior to be accurate. We utilize visualization of ranks cumulative density function in comparison to the uniform distribution, and also utilize the one-sample Kolmogorov–Smirnov test to check whether the ranks drawn from the estimated posterior follow the normal distribution. In addition, we utilize Classifier 2-Sample Test (C2ST) to compare the estimated posterior to the prior distributions[59]. We utilized the python *sbi* package implementation of C2ST, which utilizes a binary MLP classifier to distinguish samples from the estimated posterior $\theta \sim \mathbf{q}(\theta|\mathbf{x})$ and the reference posterior $\theta \sim \mathbf{p}(\theta|\mathbf{x})$. The subsequent test accuracy of the classifier ranges from 0.5, indicating that if accuracy is not better than chance then the ensembles are drawn from the same distribution, to 1 where the distributions are exactly distinguishable.

4.7 Evaluating Association of Temporal Evolution of SGM Parameters with Age

To evaluate the dynamics of SGM parameters over time during development, we tested for the correlation of SGM parameters with age. For each subject, the mean value of the inferred SGM parameter posterior distribution was selected. We then used Pearson Product-Moment Correlation to evaluate the linear association between age (log years) and SGM parameters α , S , G_{EI} , and G_{II} . Next, we sought to validate our modeling approach by evaluating the ability of SGM parameters obtained automatically via SBI to predict age, PDR, and the aperiodic exponent. We regressed

predicted vs observed values, on the x and y axes, respectively, following Piniero et al. for prediction of age, PDR, and aperiodic exponent[22]. The PDR and aperiodic exponent were automatically detected using the FOOF Python package as demonstrated in Supplementary Figure 1A[91]. We utilized a polynomial regression model (degree=2) with k-fold cross-validation (k=10). This model selection was motivated by the presence of nonlinear changes in different brain parameters over time. Such nonlinear dynamics in brain development have been recently modeled using polynomial approaches [109]. Prior functional connectivity studies have also tended to model nonlinearity with polynomial regression[124]. Age-related differences in resting-state functional connectivity from childhood to adolescence. *Cerebral Cortex* 2023). SGM parameters used in the regression model included those found to correlate with age, including α , S , and E:I gains. During each cross-validation fold, the polynomial regression model is fit to the training set containing these SGM parameters, and their mean square error (MSE) in age prediction and coefficient of determination is calculated on the held-out set.

5 Data Availability

EEG data were obtained from publicly available neonatal and infant EEG datasets with an age range of one month to one year of age[80] and publicly available database of EEGs containing ages 5 to 30 years of age[64]. The power spectra derived from the publicly available EEG samples used for simulation-based inference are available from the corresponding author upon reasonable request. EEG data for subjects between one and five years were obtained at the University of California San Francisco (UCSF) and raw patient-related data are not available due to data privacy laws. Pre-processed UCSF EEG data are available under restricted access due to ethical and privacy reasons. UCSF EEG data can be requested by contacting the corresponding author, and data sharing is conditional to the establishment of a specific data-sharing agreement between the applicant’s institution and UCSF.

6 Code Availability

Code for the spectral graph model (SGM) can be found on the spectrome package GitHub page (<https://github.com/Raj-Lab-UCSF/spectrome>). Code for incorporation of the spectral graph model (SGM) with simulation-based inference using the *sbi* Python package with examples are available on the project’s GitHub page (<https://github.com/dbernardo05/sbi-spectrome>).

References

- [1] Hans Berger. “Über das Elektroenzephalogramm des Menschen”. In: *Mittlg. Arch. Psychiatr. Nervenkr.* 98 (1932), pp. 231–254.
- [2] J Roy Smith. “The frequency growth of the human alpha rhythms during normal infancy and childhood”. In: *The Journal of Psychology* 11.1 (1941), pp. 177–198.
- [3] Orvar Eeg-Olofsson, Ingemar Petersén, and Ulla Selldén. “The Development of the Electroencephalogram in Normal Children from the Age of 1 Through 15 Years—Paroxysmal activity”. In: *Neuropädiatrie* 2.04 (1971), pp. 375–404.
- [4] Simon Duane et al. “Hybrid monte carlo”. In: *Physics letters B* 195.2 (1987), pp. 216–222.
- [5] NS Galkina and AI Boravova. “The Formation of EEG Mu-and Alpha-Rhythms in Children during the Second-Third Years of Life”. In: *Human Physiology* 22.5 (1996), pp. 540–545.
- [6] Joshua H Singer et al. “Development of glycinergic synaptic transmission to rat brain stem motoneurons”. In: *Journal of Neurophysiology* 80.5 (1998), pp. 2608–2620.
- [7] Tatiana A Stroganova, Elena V Orekhova, and Irina N Posikera. “EEG alpha rhythm in infants”. In: *Clinical Neurophysiology* 110.6 (1999), pp. 997–1012.

- [8] Olaf Sporns, Giulio Tononi, and Gerald M Edelman. “Theoretical neuroanatomy: relating anatomical and functional connectivity in graphs and cortical connection matrices”. In: *Cerebral cortex* 10.2 (2000), pp. 127–141.
- [9] P. A. Robinson et al. “Prediction of electroencephalographic spectra from neurophysiology”. In: *Phys Rev E Stat Nonlin Soft Matter Phys* 63.2 Pt 1 (2001), p. 021903.
- [10] Indu Joshi and Lu-Yang Wang. “Developmental profiles of glutamate receptors and synaptic transmission at a single synapse in the mouse auditory brainstem”. In: *The Journal of physiology* 540.3 (2002), pp. 861–873.
- [11] Peter J Marshall, Yair Bar-Haim, and Nathan A Fox. “Development of the EEG from 5 months to 4 years of age”. In: *Clinical Neurophysiology* 113.8 (2002), pp. 1199–1208.
- [12] Olivier David and Karl J Friston. “A neural mass model for MEG/EEG:: coupling and neuronal dynamics”. In: *NeuroImage* 20.3 (2003), pp. 1743–1755.
- [13] Paul Gustafson et al. “On Model Expansion, Model Contraction, Identifiability and Prior Information: Two Illustrative Scenarios Involving Mismeasured Variables [with Comments and Rejoinder]”. In: *Statistical Science* (2005), pp. 111–140.
- [14] Takao K Hensch. “Critical period plasticity in local cortical circuits”. In: *Nature Reviews Neuroscience* 6.11 (2005), pp. 877–888.
- [15] Takao K Hensch and Michela Fagiolini. “Excitatory–inhibitory balance and critical period plasticity in developing visual cortex”. In: *Progress in brain research* 147 (2005), pp. 115–124.
- [16] Maki Koike-Tani, Naoto Saitoh, and Tomoyuki Takahashi. “Mechanisms underlying developmental speeding in AMPA-EPSC decay time at the calyx of Held”. In: *Journal of Neuroscience* 25.1 (2005), pp. 199–207.
- [17] Albert Tarantola. *Inverse problem theory and methods for model parameter estimation*. SIAM, 2005.
- [18] Daniel A Spielman. “Spectral graph theory and its applications”. In: *48th Annual IEEE Symposium on Foundations of Computer Science (FOCS’07)*. IEEE, 2007, pp. 29–38.
- [19] Thomas J Whitford et al. “Brain maturation in adolescence: concurrent changes in neuroanatomy and neurophysiology”. In: *Human brain mapping* 28.3 (2007), pp. 228–237.
- [20] Roberto F Galán. “On how network architecture determines the dominant patterns of spontaneous neural activity”. In: *PloS one* 3.5 (2008), e2148.
- [21] Guillermo Gonzalez-Burgos et al. “Functional maturation of excitatory synapses in layer 3 pyramidal neurons during postnatal development of the primate prefrontal cortex”. In: *Cerebral Cortex* 18.3 (2008), pp. 626–637.
- [22] Gervasio Piñeiro et al. “How to evaluate models: observed vs. predicted or predicted vs. observed?” In: *Ecological Modelling* 216.3-4 (2008), pp. 316–322.
- [23] Mark S Scher. “Ontogeny of EEG-sleep from neonatal through infancy periods”. In: *Sleep medicine* 9.6 (2008), pp. 615–636.

- [24] C. Bédard and A. Destexhe. “Macroscopic models of local field potentials and the apparent 1/f noise in brain activity”. In: *Biophys J* 96.7 (2009), pp. 2589–2603.
- [25] Jessica S Damoiseaux and Michael D Greicius. “Greater than the sum of its parts: a review of studies combining structural connectivity and resting-state functional connectivity”. In: *Brain Structure and Function* 213.6 (2009), pp. 525–533.
- [26] Christopher J Honey et al. “Predicting human resting-state functional connectivity from structural connectivity”. In: *Proceedings of the National Academy of Sciences* 106.6 (2009), pp. 2035–2040.
- [27] ShiNung Ching et al. “Thalamocortical model for a propofol-induced alpha-rhythm associated with loss of consciousness”. In: *Proceedings of the National Academy of Sciences* 107.52 (2010), pp. 22665–22670. ISSN: 0027-8424. DOI: 10.1073/pnas.1017069108. eprint: <https://www.pnas.org/content/107/52/22665.full.pdf>. URL: <https://www.pnas.org/content/107/52/22665>.
- [28] Patric Hagmann et al. “White matter maturation reshapes structural connectivity in the late developing human brain”. In: *Proceedings of the National Academy of Sciences* 107.44 (2010), pp. 19067–19072.
- [29] Klaus-Armin Nave. “Myelination and support of axonal integrity by glia”. In: *Nature* 468.7321 (2010), pp. 244–252.
- [30] Jonathan D Power et al. “The development of human functional brain networks”. In: *Neuron* 67.5 (2010), pp. 735–748.
- [31] Sidney J Segalowitz, Diane L Santesso, and Michelle K Jetha. “Electrophysiological changes during adolescence: a review”. In: *Brain and cognition* 72.1 (2010), pp. 86–100.
- [32] Gregory Z Tau and Bradley S Peterson. “Normal development of brain circuits”. In: *Neuropsychopharmacology* 35.1 (2010), pp. 147–168.
- [33] Peter J Uhlhaas et al. “Neural synchrony and the development of cortical networks”. In: *Trends in cognitive sciences* 14.2 (2010), pp. 72–80.
- [34] Pedro A Valdés-Hernández et al. “White matter architecture rather than cortical surface area correlates with the EEG alpha rhythm”. In: *Neuroimage* 49.3 (2010), pp. 2328–2339.
- [35] AKI Chiang et al. “Age trends and sex differences of alpha rhythms including split alpha peaks”. In: *Clinical Neurophysiology* 122.8 (2011), pp. 1505–1517.
- [36] Lucy Cragg et al. “Maturation of EEG power spectra in early adolescence: a longitudinal study”. In: *Developmental science* 14.5 (2011), pp. 935–943.
- [37] Edward Wallace et al. “Emergent oscillations in networks of stochastic spiking neurons”. In: *Plos one* 6.5 (2011), e14804.
- [38] Zhi Zhang, Y-Y Jiao, and Q-Q Sun. “Developmental maturation of excitation and inhibition balance in principal neurons across four layers of somatosensory cortex”. In: *Neuroscience* 174 (2011), pp. 10–25.

- [39] Rikkert Hindriks and Michel J.A.M. van Putten. “Meanfield modeling of propofol-induced changes in spontaneous EEG rhythms”. In: *NeuroImage* 60.4 (2012), pp. 2323–2334. ISSN: 1053-8119. DOI: <https://doi.org/10.1016/j.neuroimage.2012.02.042>.
- [40] Satu Palva and J Matias Palva. “Discovering oscillatory interaction networks with M/EEG: challenges and breakthroughs”. In: *Trends in cognitive sciences* 16.4 (2012), pp. 219–230.
- [41] Alexandre Gramfort et al. “MEG and EEG Data Analysis with MNE-Python”. In: *Frontiers in Neuroscience* 7.267 (2013), pp. 1–13. DOI: 10.3389/fnins.2013.00267.
- [42] Budhachandra S Khundrakpam et al. “Developmental changes in organization of structural brain networks”. In: *Cerebral Cortex* 23.9 (2013), pp. 2072–2085.
- [43] Hae-Jeong Park and Karl Friston. “Structural and functional brain networks: from connections to cognition”. In: *Science* 342.6158 (2013).
- [44] David C Van Essen et al. “The WU-Minn human connectome project: an overview”. In: *Neuroimage* 80 (2013), pp. 62–79.
- [45] Farras Abdelnour, Henning U Voss, and Ashish Raj. “Network diffusion accurately models the relationship between structural and functional brain connectivity networks”. In: *Neuroimage* 90 (2014), pp. 335–347.
- [46] Joana Cabral et al. “Exploring mechanisms of spontaneous functional connectivity in MEG: How delayed network interactions lead to structured amplitude envelopes of band-pass filtered oscillations”. In: *NeuroImage* 90 (2014), pp. 423–435. ISSN: 1053-8119. DOI: <https://doi.org/10.1016/j.neuroimage.2013.11.047>.
- [47] Jessica Dubois et al. “The early development of brain white matter: a review of imaging studies in fetuses, newborns and infants”. In: *Neuroscience* 276 (2014), pp. 48–71.
- [48] Joaquín Goñi et al. “Resting-brain functional connectivity predicted by analytic measures of network communication”. In: *Proceedings of the National Academy of Sciences* 111.2 (2014), pp. 833–838.
- [49] Mingshan Xue, Bassam V Atallah, and Massimo Scanziani. “Equalizing excitation–inhibition ratios across visual cortical neurons”. In: *Nature* 511.7511 (2014), pp. 596–600.
- [50] Adam R Brown et al. “Developmentally regulated neurosteroid synthesis enhances GABAergic neurotransmission in mouse thalamocortical neurones”. In: *The Journal of Physiology* 593.1 (2015), pp. 267–284.
- [51] R Douglas Fields. “A new mechanism of nervous system plasticity: activity-dependent myelination”. In: *Nature Reviews Neuroscience* 16.12 (2015), pp. 756–767.
- [52] Robert C Froemke. “Plasticity of cortical excitatory-inhibitory balance”. In: *Annual review of neuroscience* 38 (2015), pp. 195–219.
- [53] Vladimir Miskovic et al. “Developmental changes in spontaneous electrocortical activity and network organization from early to late childhood”. In: *Neuroimage* 118 (2015), pp. 237–247.

- [54] Sacha B Nelson and Vera Valakh. “Excitatory/inhibitory balance and circuit homeostasis in autism spectrum disorders”. In: *Neuron* 87.4 (2015), pp. 684–698.
- [55] Martijn P Van Den Heuvel et al. “The neonatal connectome during preterm brain development”. In: *Cerebral cortex* 25.9 (2015), pp. 3000–3013.
- [56] Bradley Voytek et al. “Age-related changes in 1/f neural electrophysiological noise”. In: *Journal of Neuroscience* 35.38 (2015), pp. 13257–13265.
- [57] Selen Atasoy, Isaac Donnelly, and Joel Pearson. “Human brain networks function in connectome-specific harmonic waves”. In: *Nature Communications* 7.1 (2016), p. 10340. ISSN: 2041-1723. DOI: 10.1038/ncomms10340. URL: <http://www.nature.com/articles/ncomms10340>.
- [58] Wynn Legon et al. “Altered prefrontal excitation/inhibition balance and prefrontal output: markers of aging in human memory networks”. In: *Cerebral Cortex* 26.11 (2016), pp. 4315–4326.
- [59] David Lopez-Paz and Maxime Oquab. “Revisiting classifier two-sample tests”. In: *arXiv preprint arXiv:1610.06545* (2016).
- [60] Jil Meier et al. “A Mapping Between Structural and Functional Brain Networks”. In: *Brain Connectivity* 6.4 (2016), pp. 298–311. DOI: 10.1089/brain.2015.0408. eprint: <https://doi.org/10.1089/brain.2015.0408>. URL: <https://doi.org/10.1089/brain.2015.0408>.
- [61] Peter A Robinson et al. “Eigenmodes of brain activity: Neural field theory predictions and comparison with experiment”. In: *Neuroimage* 142 (2016), pp. 79–98.
- [62] John C Silbereis et al. “The cellular and molecular landscapes of the developing human central nervous system”. In: *Neuron* 89.2 (2016), pp. 248–268.
- [63] Samuel G Thorpe, Erin N Cannon, and Nathan A Fox. “Spectral and source structural development of mu and alpha rhythms from infancy through adulthood”. In: *Clinical Neurophysiology* 127.1 (2016), pp. 254–269.
- [64] Lindsay M Alexander et al. “An open resource for transdiagnostic research in pediatric mental health and learning disorders”. In: *Scientific data* 4 (2017), p. 170181.
- [65] Michael Breakspear. “Dynamic models of large-scale brain activity”. In: *Nature neuroscience* 20.3 (2017), pp. 340–352.
- [66] Richard Gao, Erik J Peterson, and Bradley Voytek. “Inferring synaptic excitation/inhibition balance from field potentials”. In: *Neuroimage* 158 (2017), pp. 70–78.
- [67] Xiujuan Geng et al. “Structural and maturational covariance in early childhood brain development”. In: *Cerebral Cortex* 27.3 (2017), pp. 1795–1807.
- [68] Emer J Hughes et al. “A dedicated neonatal brain imaging system”. In: *Magnetic resonance in medicine* 78.2 (2017), pp. 794–804.
- [69] Aiman S Saab and Klaus-Armin Nave. “Myelin dynamics: protecting and shaping neuronal functions”. In: *Current opinion in neurobiology* 47 (2017), pp. 104–112.

- [70] Vasily A Vakorin et al. “Developmental changes in neuromagnetic rhythms and network synchrony in autism”. In: *Annals of Neurology* 81.2 (2017), pp. 199–211.
- [71] Farras Abdelnour et al. “Functional brain connectivity is predictable from anatomic network’s Laplacian eigen-structure”. In: *NeuroImage* 172 (2018), pp. 728–739.
- [72] Cassiano O Becker et al. “Spectral mapping of brain functional connectivity from diffusion imaging”. In: *Scientific reports* 8.1 (2018), pp. 1–15.
- [73] Michael Betancourt. “Calibrating model-based inferences and decisions”. In: *arXiv preprint arXiv:1803.08393* (2018).
- [74] Yuri Bozzi, Giovanni Provenzano, and Simona Casarosa. “Neurobiological bases of autism–epilepsy comorbidity: a focus on excitation/inhibition imbalance”. In: *European Journal of Neuroscience* 47.6 (2018), pp. 534–548.
- [75] Xiaoming Du et al. “TMS evoked N100 reflects local GABA and glutamate balance”. In: *Brain stimulation* 11.5 (2018), pp. 1071–1079.
- [76] John H Gilmore, Rebecca C Knickmeyer, and Wei Gao. “Imaging structural and functional brain development in early childhood”. In: *Nature Reviews Neuroscience* 19.3 (2018), p. 123.
- [77] Meysam Hashemi et al. “Optimal model parameter estimation from EEG power spectrum features observed during general anesthesia”. In: *Neuroinformatics* 16 (2018), pp. 231–251.
- [78] Leland McInnes, John Healy, and James Melville. “Umap: Uniform manifold approximation and projection for dimension reduction”. In: *arXiv preprint arXiv:1802.03426* (2018).
- [79] Sean Talts et al. “Validating Bayesian inference algorithms with simulation-based calibration”. In: *arXiv preprint arXiv:1804.06788* (2018).
- [80] Ran Xiao et al. “Electroencephalography power and coherence changes with age and motor skill development across the first half year of life”. In: *PloS one* 13.1 (2018), e0190276.
- [81] Gaute T Einevoll et al. “The scientific case for brain simulations”. In: *Neuron* 102.4 (2019), pp. 735–744.
- [82] David Greenberg, Marcel Nonnenmacher, and Jakob Macke. “Automatic posterior transformation for likelihood-free inference”. In: *International Conference on Machine Learning*. PMLR, 2019, pp. 2404–2414.
- [83] Maria Giulia Preti and Dimitri Van De Ville. “Decoupling of brain function from structure reveals regional behavioral specialization in humans”. In: *Nature Communications* 10.1 (2019). arXiv: 1905.07813. ISSN: 20411723. DOI: 10.1038/s41467-019-12765-7. URL: <https://doi.org/10.1038/s41467-019-12765-7> (visited on 11/24/2019).
- [84] Vikaas S Sohal and John LR Rubenstein. “Excitation-inhibition balance as a framework for investigating mechanisms in neuropsychiatric disorders”. In: *Molecular psychiatry* 24.9 (2019), pp. 1248–1257.
- [85] Prejaas Tewarie et al. “How do spatially distinct frequency specific MEG networks emerge from one underlying structural connectome? The role of the structural eigenmodes”. In: *NeuroImage* 186 (2019), pp. 211–220.

- [86] Cleber A Trujillo et al. “Complex oscillatory waves emerging from cortical organoids model early human brain network development”. In: *Cell stem cell* 25.4 (2019), pp. 558–569.
- [87] Graham L Baum et al. “Development of structure–function coupling in human brain networks during youth”. In: *Proceedings of the National Academy of Sciences* 117.1 (2020), pp. 771–778.
- [88] Kyle Cranmer, Johann Brehmer, and Gilles Louppe. “The frontier of simulation-based inference”. In: *Proceedings of the National Academy of Sciences* 117.48 (2020), pp. 30055–30062.
- [89] Koen Cuypers and Anouk Marsman. “Transcranial magnetic stimulation and magnetic resonance spectroscopy: Opportunities for a bimodal approach in human neuroscience”. In: *Neuroimage* (2020), p. 117394.
- [90] Samuel Deslauriers-Gauthier et al. “A unified framework for multimodal structure-function mapping based on eigenmodes”. In: *Medical Image Analysis* 66 (2020), p. 101799. eprint: doi:10.1016/j.media.2020.101799.
- [91] Thomas Donoghue et al. “Parameterizing neural power spectra into periodic and aperiodic components”. In: *Nature neuroscience* 23.12 (2020), pp. 1655–1665.
- [92] Katharina Glomb et al. “Connectome spectral analysis to track EEG task dynamics on a subsecond scale”. In: *NeuroImage* (2020), p. 117137.
- [93] Pedro J Gonçalves et al. “Training deep neural density estimators to identify mechanistic models of neural dynamics”. In: *Elife* 9 (2020), e56261.
- [94] Meysam Hashemi et al. “The Bayesian Virtual Epileptic Patient: A probabilistic framework designed to infer the spatial map of epileptogenicity in a personalized large-scale brain model of epilepsy spread”. In: *NeuroImage* 217 (2020), p. 116839.
- [95] Joeri Hermans, Volodimir Begy, and Gilles Louppe. “Likelihood-free mcmc with amortized approximate ratio estimators”. In: *International conference on machine learning*. PMLR, 2020, pp. 4239–4248.
- [96] Samuel A Neymotin et al. “Human Neocortical Neurosolver (HNN), a new software tool for interpreting the cellular and network origin of human MEG/EEG data”. In: *Elife* 9 (2020), e51214.
- [97] Ashish Raj et al. “Spectral graph theory of brain oscillations”. In: *Human Brain Mapping* (2020).
- [98] Golia Shafiei et al. “Topographic gradients of intrinsic dynamics across neocortex”. In: *Elife* 9 (2020), e62116.
- [99] Alvaro Tejero-Cantero et al. “sbi: A toolkit for simulation-based inference”. In: *Journal of Open Source Software* 5.52 (2020), p. 2505. DOI: 10.21105/joss.02505. URL: <https://doi.org/10.21105/joss.02505>.
- [100] Prejaas Tewarie et al. “Mapping functional brain networks from the structural connectome: Relating the series expansion and eigenmode approaches”. In: *Neuroimage* 216 (2020), p. 116805. eprint: doi:10.1016/j.neuroimage.2020.116805.
- [101] Farras Abdelnour et al. “Algebraic relationship between the structural network’s Laplacian and functional network’s adjacency matrix is preserved in temporal lobe epilepsy subjects”. In: *NeuroImage* 228 (2021), p. 117705.

- [102] Adriana Caballero, Amanda Orozco, and Kuei Y Tseng. “Developmental regulation of excitatory-inhibitory synaptic balance in the prefrontal cortex during adolescence”. In: *Seminars in Cell & Developmental Biology*. Vol. 118. Elsevier. 2021, pp. 60–63.
- [103] Joeri Hermans et al. “A trust crisis in simulation-based inference? your posterior approximations can be unfaithful”. In: *arXiv preprint arXiv:2110.06581* (2021).
- [104] Bo-yong Park et al. “Signal diffusion along connectome gradients and inter-hub routing differentially contribute to dynamic human brain function”. In: *NeuroImage* 224 (2021), p. 117429.
- [105] Pedro Rodrigues et al. “HNPE: Leveraging global parameters for neural posterior estimation”. In: *Advances in Neural Information Processing Systems* 34 (2021), pp. 13432–13443.
- [106] Natalie Schaworonkow and Bradley Voytek. “Longitudinal changes in aperiodic and periodic activity in electrophysiological recordings in the first seven months of life”. In: *Developmental cognitive neuroscience* 47 (2021), p. 100895.
- [107] Valerie J Sydnor et al. “Neurodevelopment of the association cortices: Patterns, mechanisms, and implications for psychopathology”. In: *Neuron* 109.18 (2021), pp. 2820–2846.
- [108] Xihe Xie et al. “Emergence of canonical functional networks from the structural connectome”. In: *NeuroImage* 237 (2021), p. 118190.
- [109] Richard AI Bethlehem et al. “Brain charts for the human lifespan”. In: *Nature* 604.7906 (2022), pp. 525–533.
- [110] Judit Ciarrusta et al. “The developing brain structural and functional connectome fingerprint”. In: *Developmental Cognitive Neuroscience* 55 (2022), p. 101117.
- [111] Michael Deistler, Pedro J Goncalves, and Jakob H Macke. “Truncated proposals for scalable and hassle-free simulation-based inference”. In: *Advances in Neural Information Processing Systems* 35 (2022), pp. 23135–23149.
- [112] Denis A Engemann et al. “A reusable benchmark of brain-age prediction from M/EEG resting-state signals”. In: *Neuroimage* 262 (2022), p. 119521.
- [113] Aron T Hill et al. “Periodic and Aperiodic Neural Activity Displays Age-Dependent Changes Across Early-to-Middle Childhood”. In: *Developmental Cognitive Neuroscience* (2022), p. 101076.
- [114] Dan Hu et al. “Existence of functional connectome fingerprint during infancy and its stability over months”. In: *Journal of Neuroscience* 42.3 (2022), pp. 377–389.
- [115] Kamalini G Ranasinghe et al. “Altered excitatory and inhibitory neuronal subpopulation parameters are distinctly associated with tau and amyloid in Alzheimer’s disease”. In: *Elife* 11 (2022), e77850.
- [116] Jocelyn Urrutia-Piñones et al. “Long-range gabaergic projections of cortical origin in brain function”. In: *Frontiers in Systems Neuroscience* 16 (2022), p. 841869.
- [117] Daniel Ward et al. “Robust neural posterior estimation and statistical model criticism”. In: *Advances in Neural Information Processing Systems* 35 (2022), pp. 33845–33859.

- [118] Farnaz Zamani Esfahlani et al. “Local structure-function relationships in human brain networks across the lifespan”. In: *Nature communications* 13.1 (2022), p. 2053.
- [119] Paul-Christian Bürkner, Maximilian Scholz, and Stefan T Radev. “Some models are useful, but how do we know which ones? Towards a unified Bayesian model taxonomy”. In: *Statistic Surveys* 17 (2023), pp. 216–310.
- [120] Meysam Hashemi et al. “Amortized Bayesian inference on generative dynamical network models of epilepsy using deep neural density estimators”. In: *Neural Networks* 163 (2023), pp. 178–194.
- [121] Huaqing Jin et al. “Bayesian inference of a spectral graph model for brain oscillations”. In: *NeuroImage* 279 (2023), p. 120278.
- [122] Mario Lavanga et al. “The virtual aging brain: Causal inference supports interhemispheric dedifferentiation in healthy aging”. In: *NeuroImage* 283 (2023), p. 120403.
- [123] Erfan Nozari et al. “Macroscopic resting-state brain dynamics are best described by linear models”. In: *Nature Biomedical Engineering* (2023), pp. 1–17.
- [124] Ashley FP Sanders et al. “Age-related differences in resting-state functional connectivity from childhood to adolescence”. In: *Cerebral Cortex* 33.11 (2023), pp. 6928–6942.
- [125] Parul Verma, Srikantan Nagarajan, and Ashish Raj. “Stability and dynamics of a spectral graph model of brain oscillations”. In: *Network Neuroscience* 7.1 (2023), pp. 48–72.
- [126] Daolang Huang et al. “Learning Robust Statistics for Simulation-based Inference under Model Misspecification”. In: *Advances in Neural Information Processing Systems* 36 (2024).

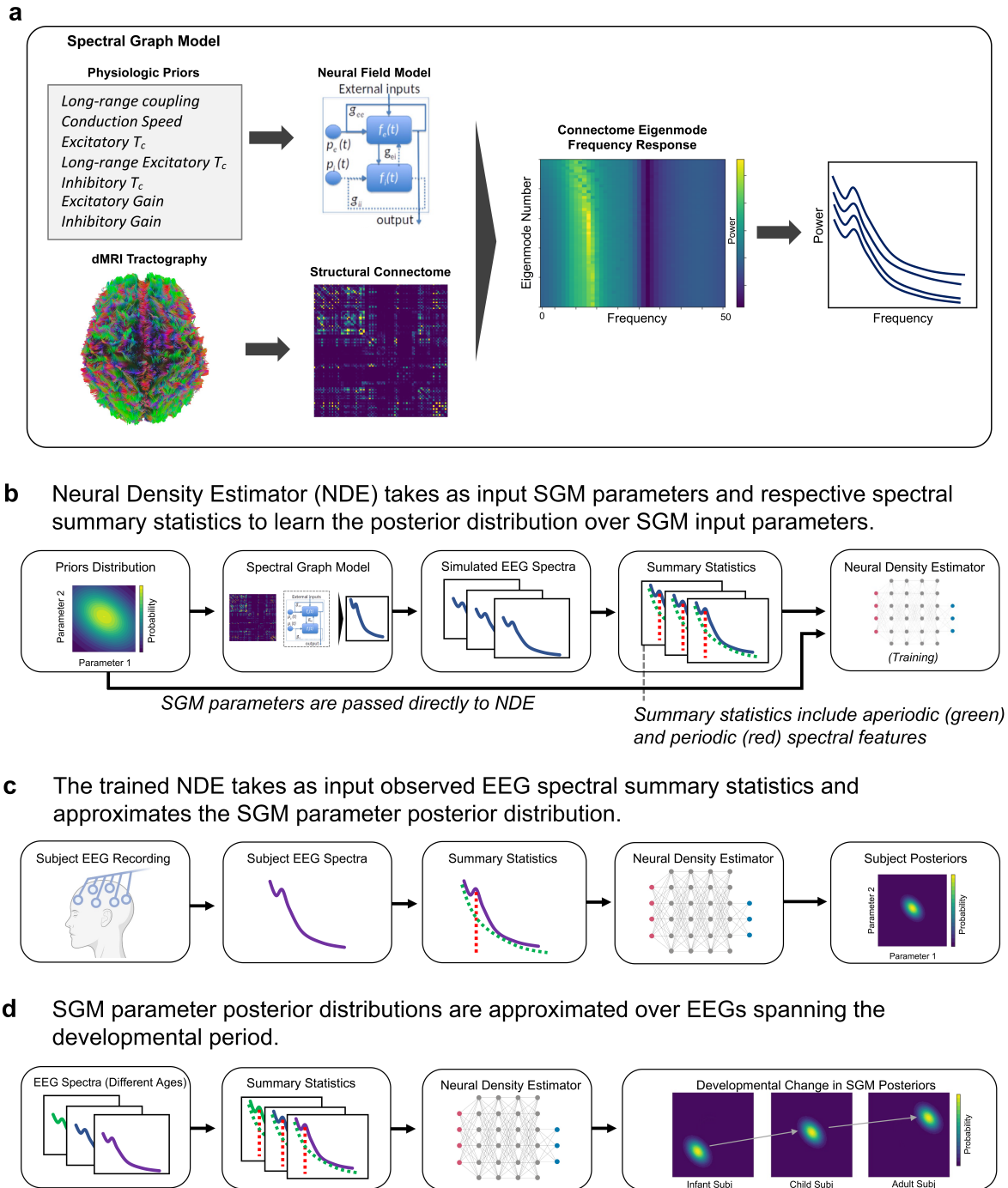
7 Tables

Table 1: SGM parameters and bounds

Name	Symbol	Bounds
Excitatory time constant	τ_e	[0.001, 0.03]
Inhibitory time constant	τ_i	[0.001, 0.03]
Long-range coupling constant	α	[0.01, 1.0]
Conduction velocity	S	[0.5 m/s, 15 m/s]
Excitatory gain	G_{EI}	[1, 20]
Inhibitory gain	G_{II}	[1, 20]
Graph time constant	τ_G	[0.01, 0.3]

8 Figures

Figure 1: Study Overview



a) Spectral Graph Model Overview for simulation of EEG spectra from linearized neural field model modulated over eigenmodes of the structural connectome, **b)** Simulation-based Bayesian inference training of neural density estimator of the prior distribution. During training, the neural density estimator learns the association between spectral features and underlying SGM parameters. **c)** Derivation of the posterior parameter distribution given a real-world EEG recording, **d)** Derivation of population SGM parameter distributions from individuals at different developmental ages. Examples of infant, child, and adult spectra across different developmental ages are shown (real-world subject spectra are shown in Supplementary Figures 1A and 1B.) Hypothetical examples of inferred posterior distributions at infant, child, and adult ages demonstrate hypothetical developmental shifts in SGM parameters.

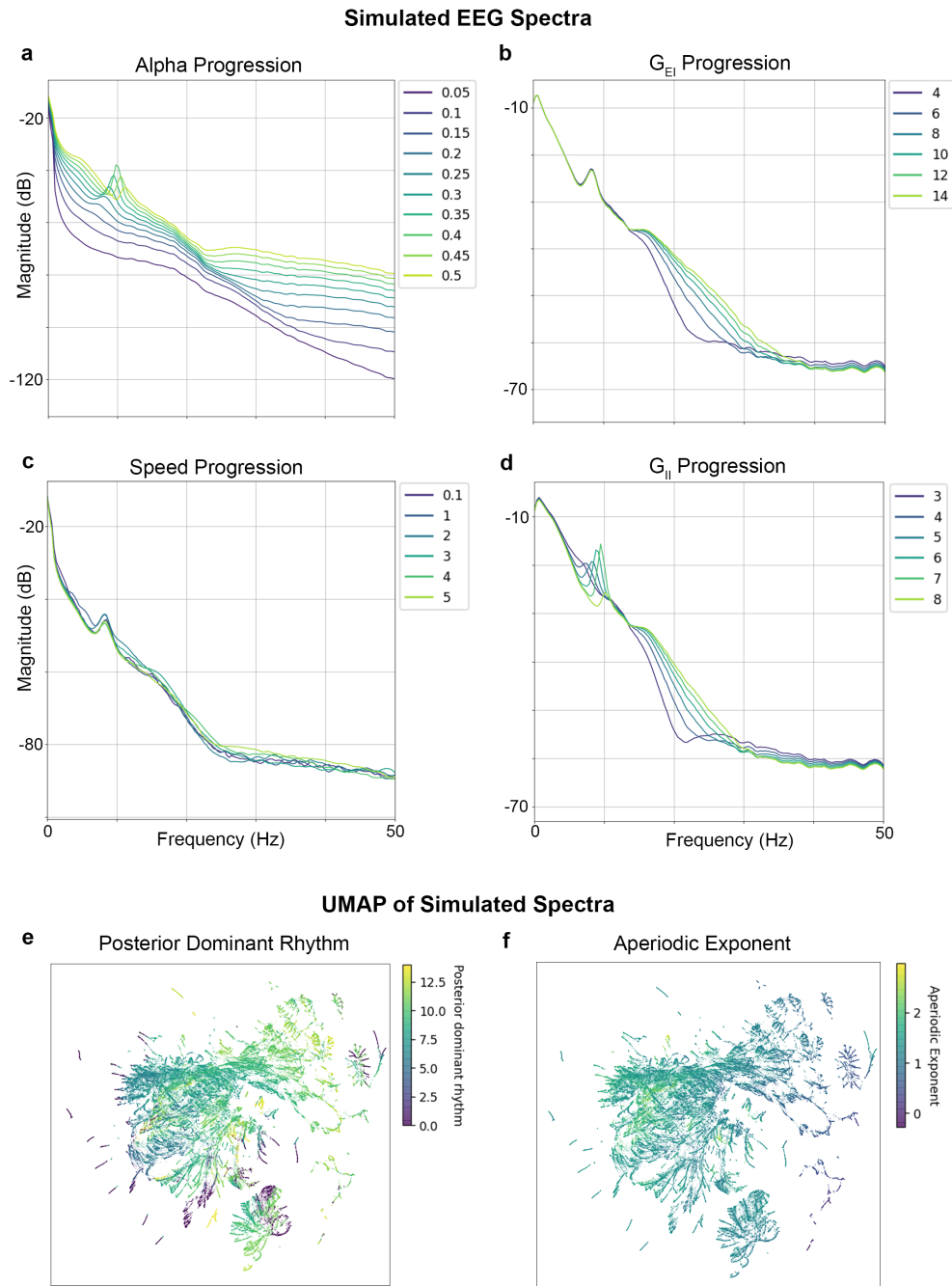
Figure 2: SGM spectral changes with different SGM parameter values

Figure 2, a-f demonstrates the effect of varying SGM parameters. **a)** α parameter progression shows emergence and increase in the frequency of posterior dominant rhythm as α is increased, **b)** Excitatory gain progression shows a change in aperiodic content of spectral frequencies greater than 10 Hz. **c)** Axonal conduction speed parameter progression shows an increase in PDR frequency as speed is increased. **d)** Inhibitory gain progression shows the emergence of PDR and increase in PDR frequency as well as changes in the aperiodic content of spectral frequencies greater than 10 Hz. **e)** UMAP embedding showing gradients in PDR frequency evident in different clusters. Spectra without PDR are shown in purple. There are regions with homogenous PDR frequency suggesting SGM parameter regimes that yield similar PDR. **f)** UMAP embedding showing gradients in aperiodic exponent evident in different clusters. There are regions with homogenous aperiodic exponents suggesting regions of SGM parameter space that yield similar aperiodic exponents.

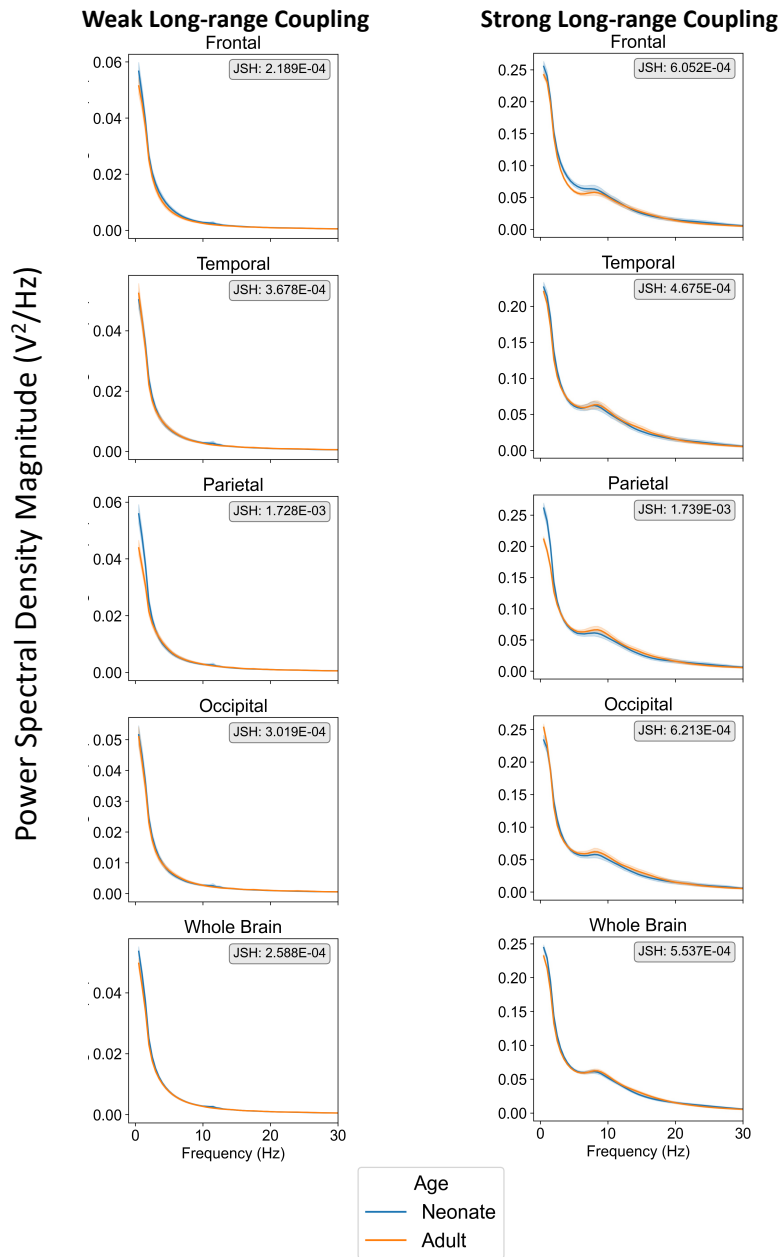
Figure 3: Effect of Neonatal versus Adult Connectome on SGM

Figure 3: We compared the differential effects of utilizing a neonatal versus adult connectome on SGM spectral realizations based on strong versus weak long-range coupling (α) across different brain regions (frontal, temporal, parietal, occipital, and whole-brain). The left column demonstrates SGM realizations with weak long-range coupling while the right column demonstrates SGM realizations with strong long-range coupling. Each plot shows SGM realizations instantiated with either group-averaged term neonatal connectomes (blue) and adult connectomes (orange). Qualitatively, there are appreciable slight augmentations in relative delta power in neonatal SGM realizations compared to adults, which are more pronounced in the parietal regions. However, quantitatively, a comparison of spectral distributions generated by the adult and neonatal connectomes within weak and strong long-range coupling regimes demonstrated only minor differences with Jensen-Shannon divergences less than 0.01.

Figure 4: Observed subject EEG spectra and their inferred SGM parameter posterior distributions and corresponding simulated spectra

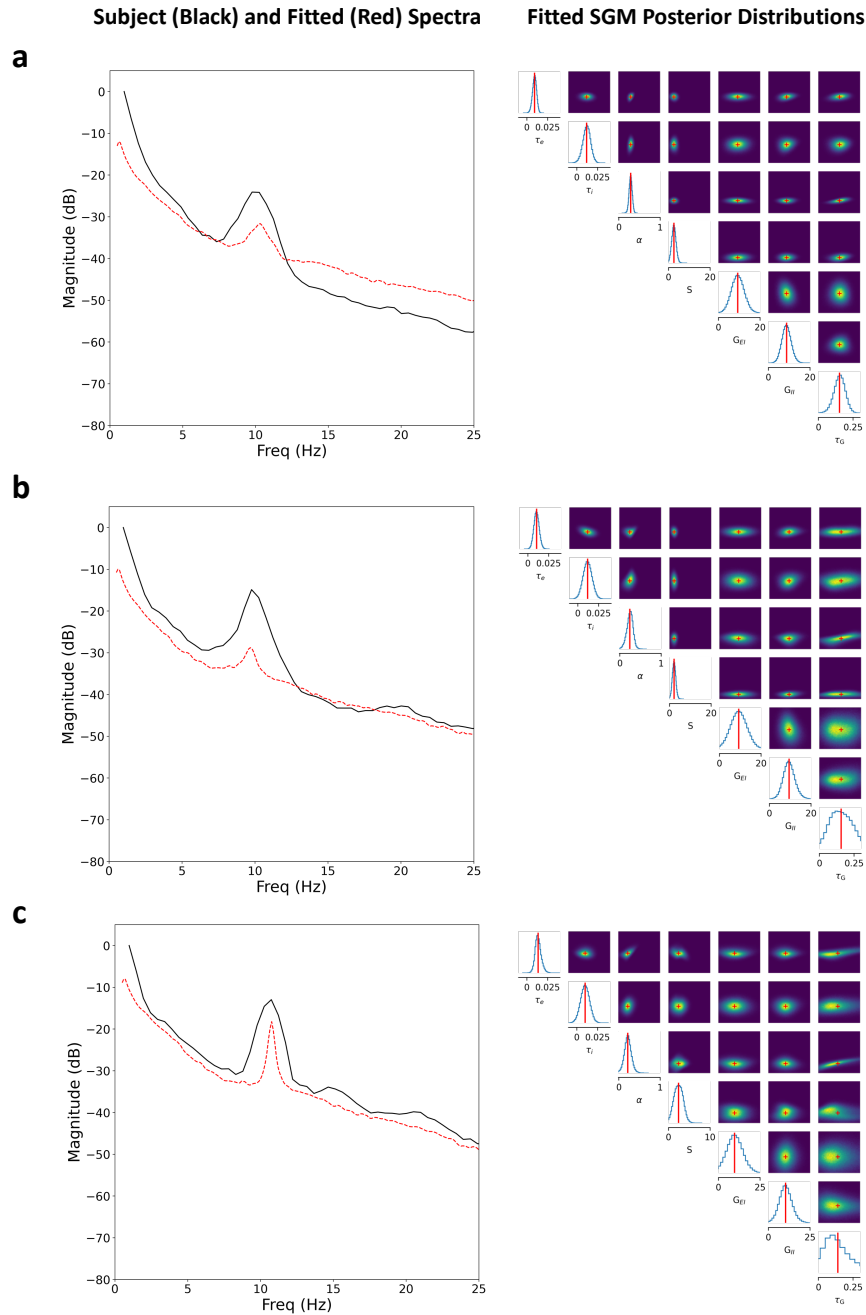


Figure 4: Examples of Simulation-based Bayesian inference (SBI) of SGM Parameter Posterior Distributions and Respective Example Subject EEG Spectrum (black) and SGM Simulated Spectrum (red). SBI was used to infer SGM parameter posterior likelihoods from observed subjects (three examples shown in a-c). Kernel density estimation (KDE) of the resulting posterior probability distribution were calculated and the mean of the KDE for each SGM variable (red cross) was used to simulate the EEG spectrum (red) with SGM for the shown example subjects.

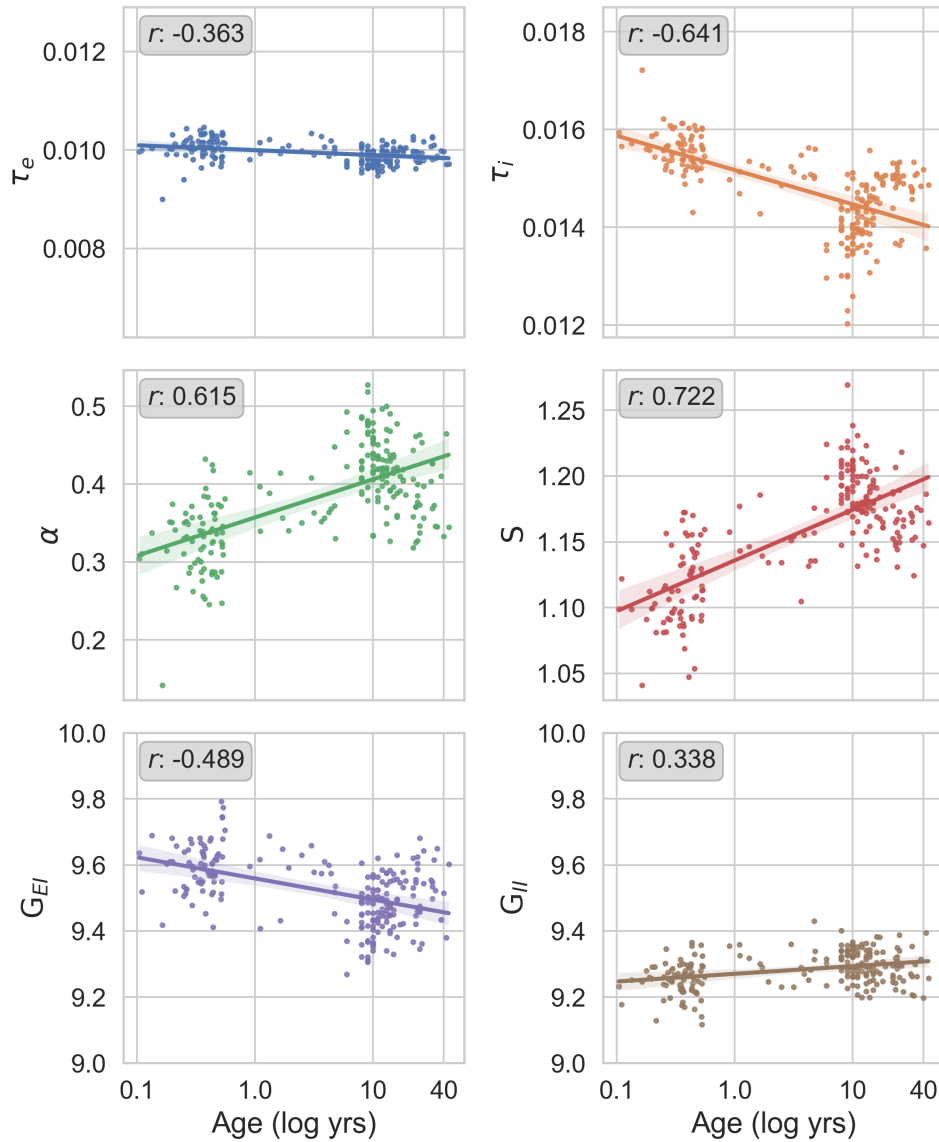
Figure 5: SBI of SGM parameters over the developmental period

Figure 5: Simulation-based Bayesian Inference (SBI) derived SGM Parameters Evolution Over Time. Each blue circle represents the peak value of the respective SGM parameter distribution (y-axis) for a respective subject, as inferred by SBI, plotted over respective age of the subject (x-axis). The linear regression model fit is represented by the solid line and the shaded area represents 95% confidence interval. **a)** α demonstrated Pearson r of 0.284 ($p = 3.88e-5$). **b)** Excitatory Gain demonstrated r of -0.430 ($p = 1.40e-10$). **c)** Axonal conduction speed demonstrated r of 0.350 ($p = 2.97e-7$). **d)** Inhibitory Gain did not demonstrate a linear correlation with age. The x-axis tick labels are log-scaled for visualization purposes.

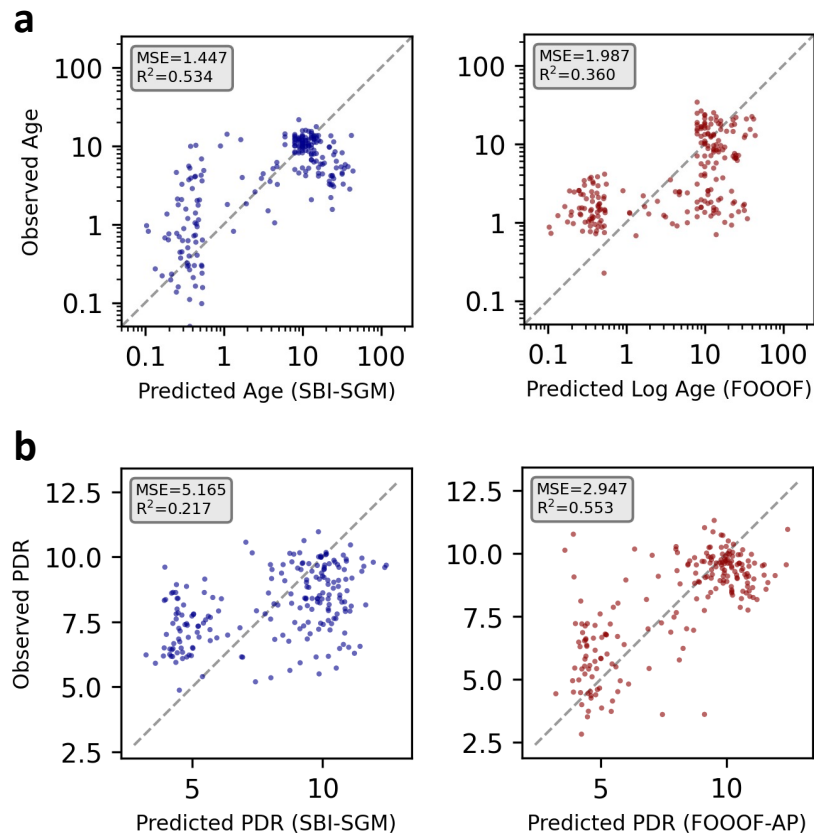
Figure 6: Prediction of Age and PDR from Inferred SGM parameters

Figure 6. a) Observed versus predicted age plots are demonstrated for predicted ages derived from linear regression models based on SBI-SGM (left panel) and Fitting Oscillations & One Over F (FOOF) models (right panel). Respective Adjusted R^2 and mean square error (MSE) values are shown in the gray subset boxes. The SBI-SGM and FOOF models demonstrated similar performance with SBI-SGM having slightly improved adjusted R^2 and mean square error (MSE) scores. b) Posterior dominant rhythm observed versus predicted with SBI-SGM versus FOOF. FOOF demonstrated improved prediction of the PDR compared to SBI-SGM.

9 Supporting Information

9.1 Parameter recovery, sensitivity analyses, and simulation based calibration analyses.

In order to assess the accuracy and robustness of the SBI-SGM inference framework, we conducted parameter recovery analyses and simulation-based calibration (SBC) with synthetic data. In the context of SBI, the efficacy of the inference may be evaluated by parameter recovery, specifically—given known ground truth parameters θ , how well does the inference procedure recover them? Running SBI on 100 synthetic SGM realizations within physiologically informed prior bounds (Table 1), we more accurately recovered SGM parameters with the NPE and TSNPE, relative to NRE (Supplementary Figure 3-6). α was the most accurately recovered parameter across all model families, whereas S and τ_G had the poorest recovery. For parameter recovery across all SGM parameters, NPE had the lowest mean relative estimated error (*REE*), 0.0451, compared to 0.0560 for TSNPE and 0.114 for NRE (Supplementary Figure 6). To evaluate potential pathologies of the SBI process, we performed Bayesian sensitivity analysis evaluating posterior z -score and posterior contraction (Supplementary Figure 7) for each parameter using NRE, NPE, and TSNPE across various simulation budget sizes [73]. We demonstrate that relative to NPE and NRE, TSNPE provided improved posterior contraction (Supplementary Figures 8 and 9). Systematic posterior underdispersion or overdispersion limited usefulness of posterior z -scores in the comparison of different model families and their respective parameterizations, particularly for NRE, whose posteriors demonstrated significantly increased posterior dispersion relative to NPE and TSNPE. We evaluated posterior dispersion indices (PDI) quantifying the degree of posterior dispersion while standardizing for the varied scale of different SGM parameters and demonstrate that NPE and TSNPE had reduced PDI relative to NRE (Supplementary Figure 10).

To evaluate the calibration of the uncertainties of the estimated posteriors, we assessed the SBC of NPE and TSNPE. NRE was excluded from SBC analysis because the NRE-based inference of SGM parameters proved computationally prohibitive due to the utilization of MCMC sampling. We found that the TSNPE yielded posteriors with well-calibrated uncertainties, whereas NPE yielded posteriors with left-skewed rank distribution consistent with systematic underestimation of the posterior means (Supplementary Figure 11). To quantify SBC, we utilized the Kolmogorov-Smirnov (KS) test to evaluate the null hypothesis that the samples from ranks are drawn from a uniform distribution. TSNPE SBC KS testing demonstrated p-values over 0.05 for all SGM parameters, which suggests the posterior distribution aligns with a uniform distribution, aligning with a necessary, though not sufficient, condition for the estimated posterior to be accurately calibrated. In contrast, KS testing for NPE across all SGM parameters demonstrated p-values < 0.001 . In addition, we performed the Classifier 2-Sample Test (C2ST) to assess whether the estimated posterior is drawn from the same distribution as the prior, and this demonstrated that the Data Averaged Posterior (DAP) compared to the prior demonstrated C2ST values between 0.473 to 0.510, approximating 0.5, indicating statistical similarity of the DAP distribution to the prior distribution. The performance differences between NPE and TSNPE are characterized by superior calibration in TSNPE and lower relative estimation error in parameter recovery for NPE.

This distinction highlights that greater accuracy in parameter estimates does not necessarily correspond to an accurate representation of true data uncertainties.

9.2 Performance differences between NRE, NPE, and TSNPE

Here, we evaluate potential sources of the differential performance observed with NRE, NPE, and TSNPE. In evaluating potential sources of error in parameter recovery and calibration, we observed a tendency for NPE to exhibit posterior mass leakage beyond the defined prior boundaries leading to clustering of posterior mass at prior boundaries, as previously reported by Deister et al[111]. NPE showed clustering of posterior mass near the boundary limits for parameters, especially with conduction speed. In contrast, TSNPE demonstrated no such leakage (Supplementary Figure 12). Despite the potential leakage, the estimated posterior within the prior bounds for NPE was accurate in capturing true parameters as evidenced by its higher REE scores; consistent with prior findings by Diestler et al. that despite leakage, the approximate posterior within the bounds of the prior may still be reflective of the true posterior[111]. However, this leakage negatively impacts the posterior distribution shape estimated by NPE, particularly impacting parameters with complex identifiability, such as conduction speed. This issue may contribute to the poorer calibration results observed with NPE compared to TSNPE. While transformations of parameter space and other remedies for NPE leakage have been proposed, Diestler et al. noted that these modifications to NPE did not sufficiently rectify the shortcomings in real-world data, whereas TSNPE effectively mitigated leakage[111]. Our findings indicate improved posterior calibration with TSNPE, aligning with the findings of Deistler et al. that TSNPE may recover posteriors with good calibration more effectively than NPE[111].

Next, upon inspection of posterior predictive checks (PPC) utilizing synthetic spectral realizations we observed that the estimated posterior distributions qualitatively demonstrated interdependencies among certain SGM parameters which varied according to SBI method utilized (Supplementary Figures 3-5). We assessed these correlations by computing Pearson correlation coefficient matrix for the joint marginal distributions (Supplementary Figure 13). There were strong correlations across several joint marginals of the estimated posterior distribution, indicative of model degeneracy, wherein multiple model parameterizations yield similar spectral realizations. NPE had increased sensitivity to detect correlations between parameters compared to TSNPE. Increasing simulation budget size with TSNPE led to increased alignment in detected significant correlations with NPE, suggesting that increased simulation budget size for neural density estimator training increases its ability to capture interdependencies in the multivariate posterior distribution. However, when averaging across the entire synthetic dataset, no significant correlations were observed. This observation suggests that while model degeneracy may explain the correlations seen in individual joint marginal distributions, it may not manifest uniformly against the variance representative of spectral developmental trajectories.

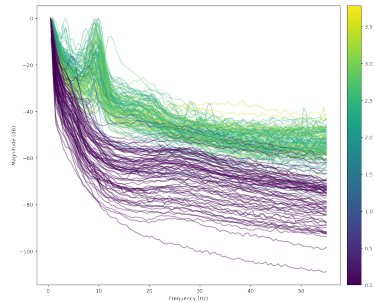
Concerning the improved REE performance of NPE compared to TSNPE, we attribute this to the larger simulation budgets allocated to NPE relative to TSNPE due to the computational efficiency of amortized inference of NPE compared to the non-amortized inference of TSNPE. Larger simulation budgets generally lead to performance gains for NPE-based methods [82]. However, for TSNPE, this comes at the expense of computational complexity that scales

linearly with the number of subjects because a new neural density estimator is learned for each subject at each inference round for TSNPE. In comparison, with NPE, a single trained neural density estimator is re-used across all subjects.

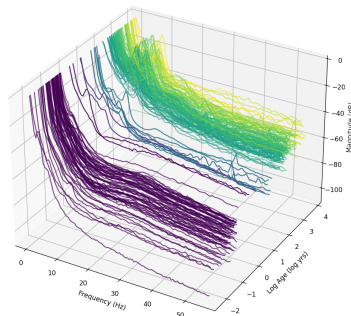
10 Supplementary Figures

Figure S1: Empirical Subject EEG Spectra

a: Subject Spectra Colored by Log Age (log years)

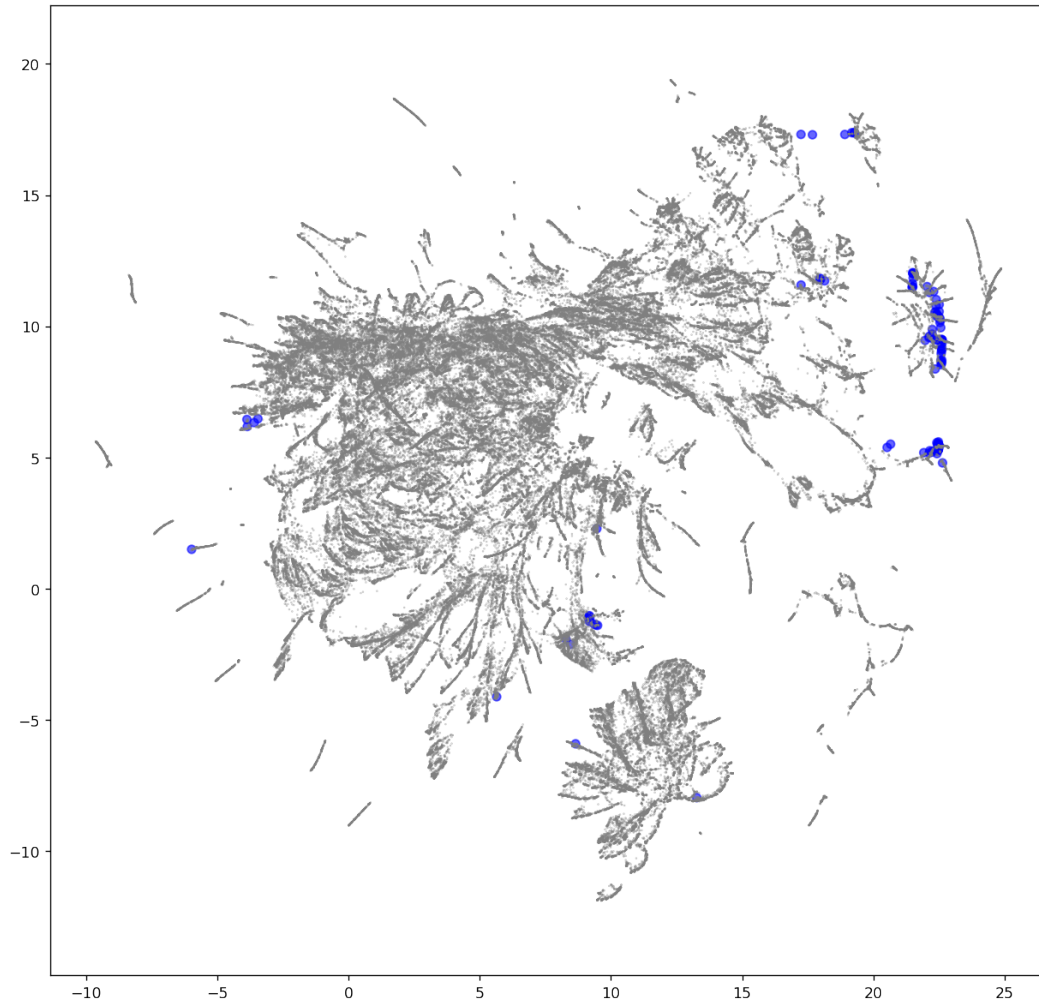


b: Subject Spectra Colored by Log Age (log years)



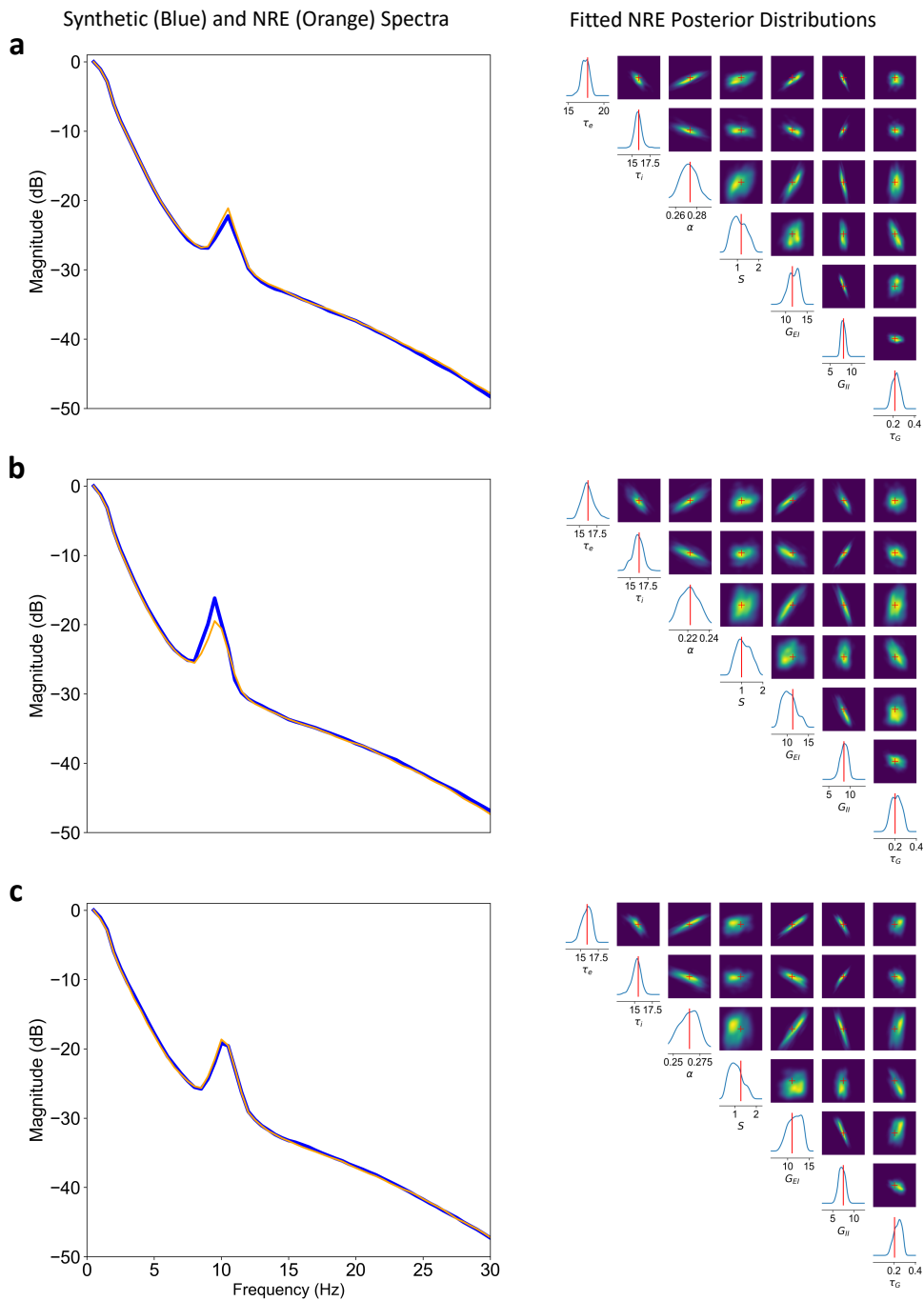
Supplementary Figure 1: a) demonstrates all subject spectra colored by age, color-mapped to log years. For visualization purposes, all spectra are scaled to the power corresponding to 0.5 to 1 Hz frequency bin. In this 3d representation, age is mapped to the z-axis in a plane perpendicular to the page. b) demonstrates all subject spectra colored by age, color-mapped to log years. For visualization purposes, all spectra are scaled to the power corresponding to 0.5 to 1 Hz frequency bin.

Figure S2: UMAP of Subjects (blue) and Simulations (grey)

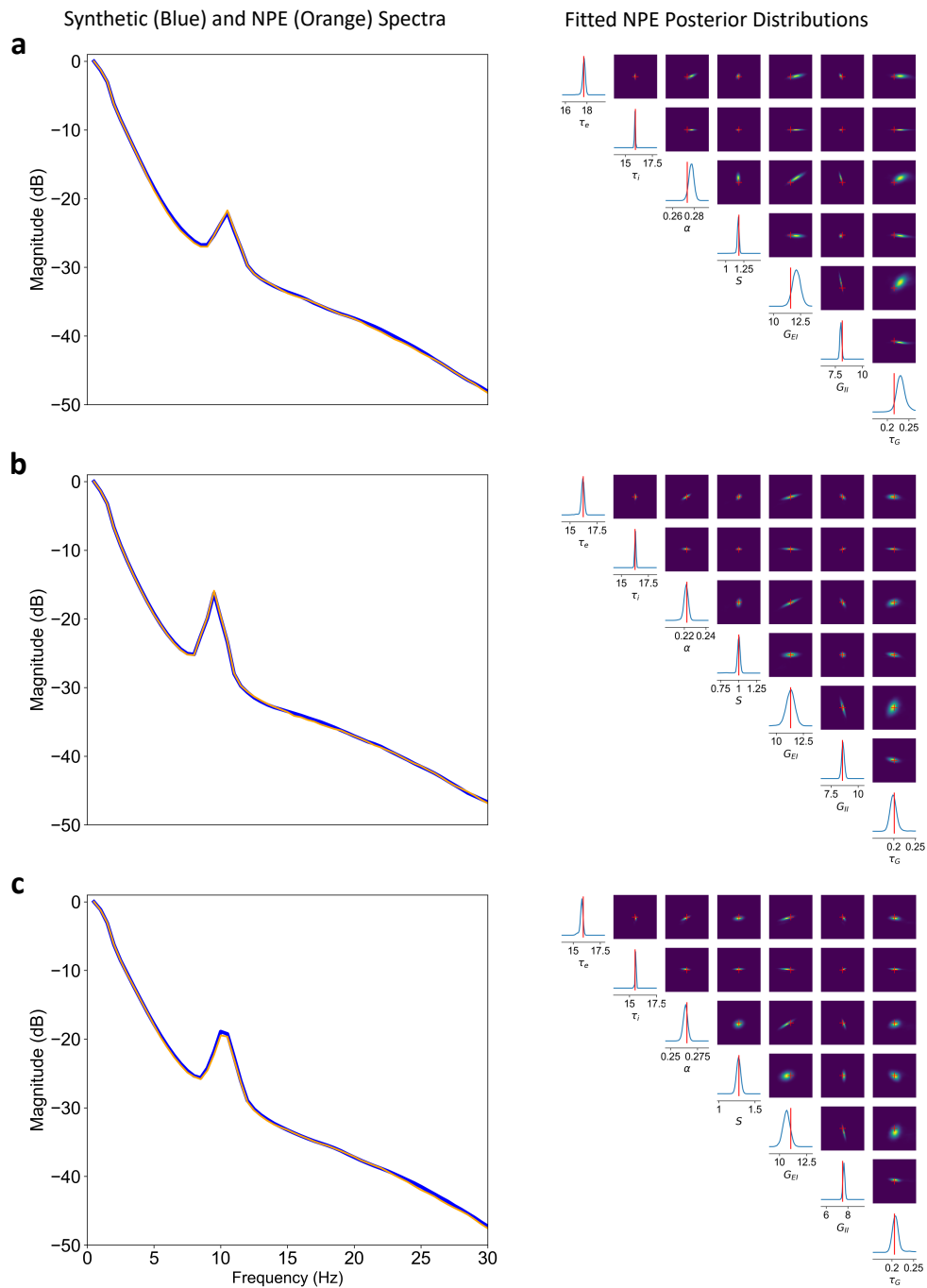


Supplementary Figure 2: UMAP embedding (N=196000 simulations) demonstrating clustering of simulation spectra with simulations colored in grey and subjects colored in blue

Figure S3: Synthetic EEG spectra and SGM parameter posterior distributions and simulated spectra inferred with NRE

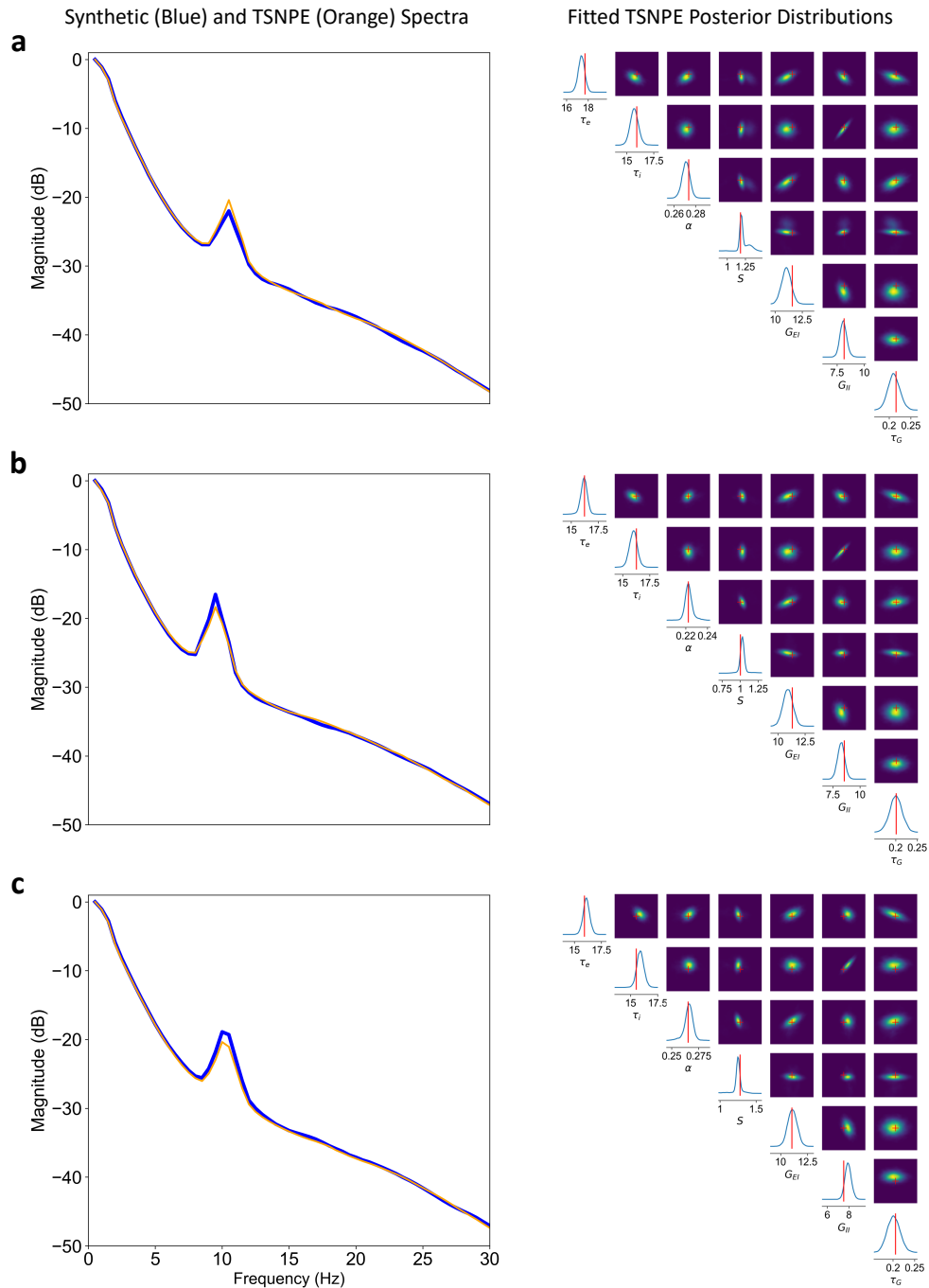


Supplementary Figure 3: Examples of Neural Ratio Estimation (NRE) of SGM Parameter Posterior Distributions and Respective Example Synthetic EEG Spectrum (black) and SGM Simulated Spectrum (red). NRE with simulation budget size of $1E6$ simulations was used to infer SGM parameter posterior likelihoods from synthetic subjects (three examples shown in **a-c**). The left column shows three examples (a-c) of synthetic (blue) and fitted EEG spectrum (blue). Kernel density estimation (KDE) of the resulting estimated posterior probability distribution and the true value for each SGM parameter (red cross) are shown on the right column.

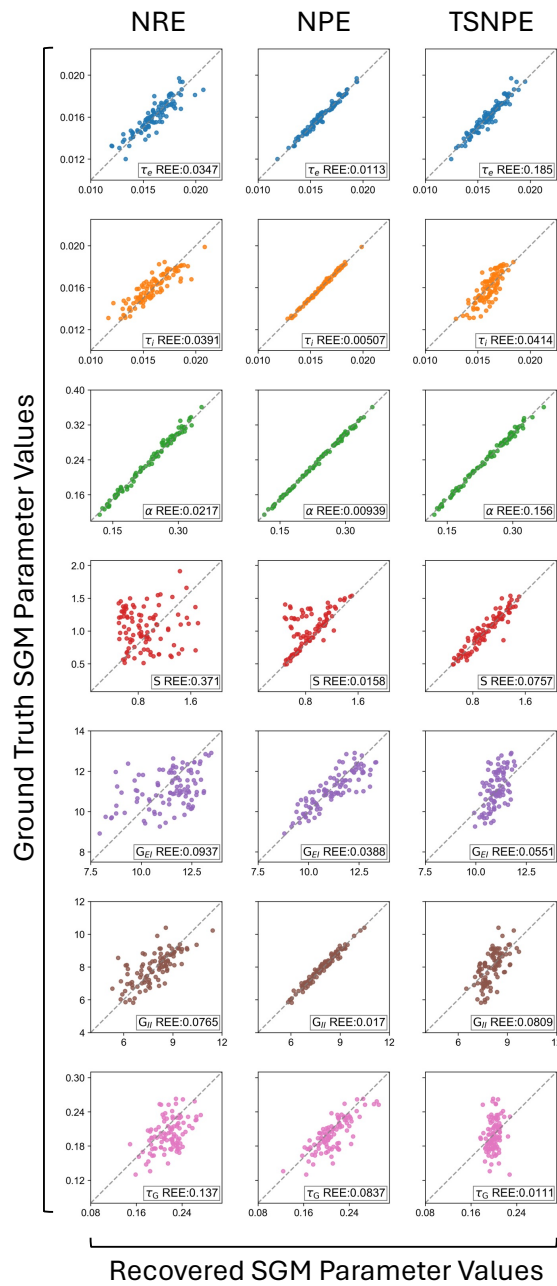
Figure S4: Synthetic EEG spectra and SGM parameter posterior distributions and simulated spectra inferred with NPE

Supplementary Figure 4: Examples of Neural Posterior Estimation (NPE) of SGM Parameter Posterior Distributions and Respective Example Synthetic EEG Spectrum (black) and SGM Simulated Spectrum (red). NPE with simulation budget of $1E6$ simulations was used to infer SGM parameter posterior likelihoods from synthetic subjects (three examples shown in **a-c**). The left column shows three examples (a-c) of synthetic (blue) and fitted EEG spectrum (blue). Kernel density estimation (KDE) of the resulting estimated posterior probability distribution and the true value for each SGM parameter (red cross) are shown on the right column.

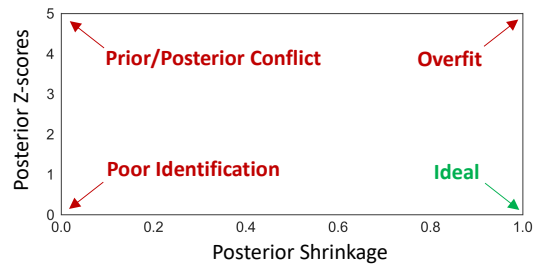
Figure S5: Synthetic EEG spectra and SGM parameter posterior distributions and simulated spectra inferred with TSNPE



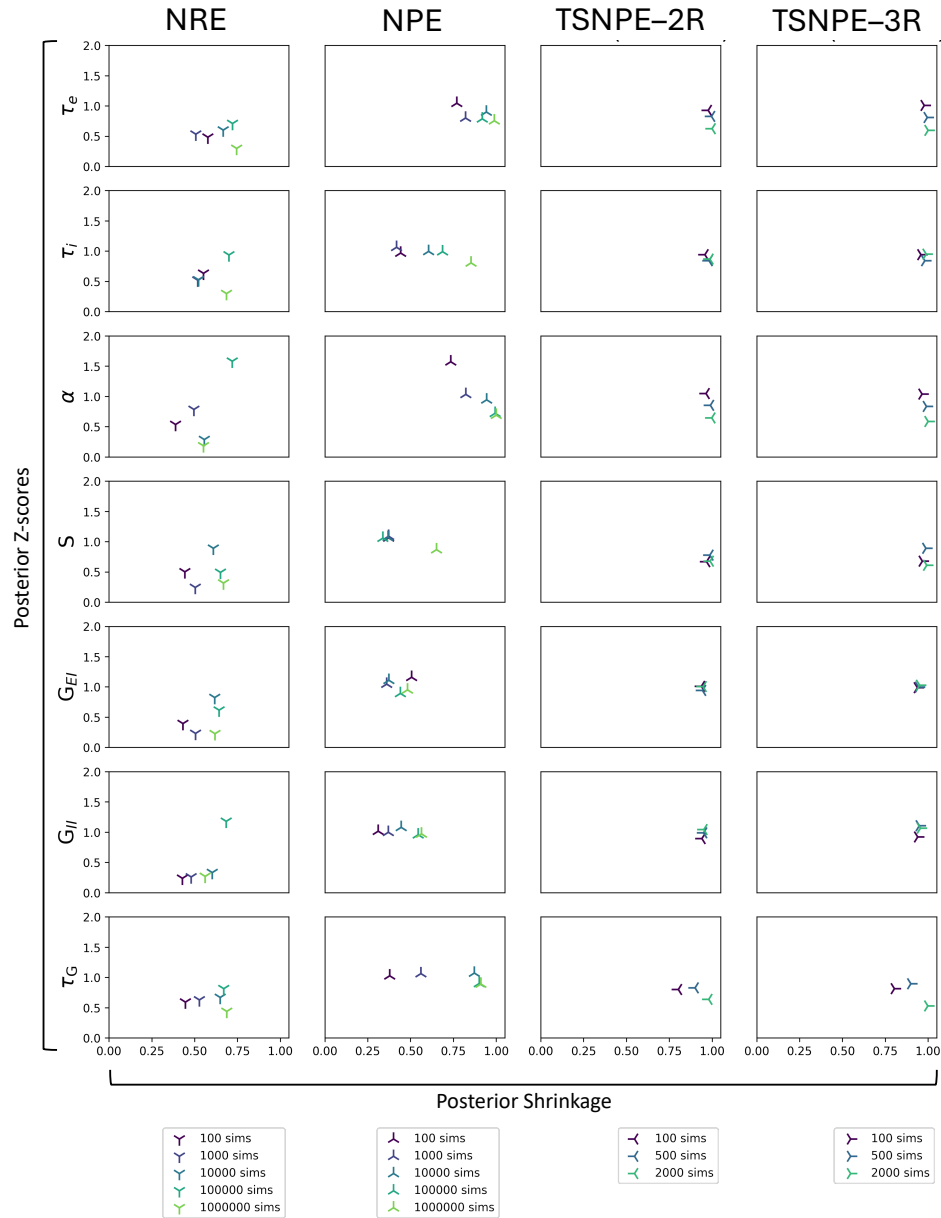
Supplementary Figure 5: Examples of Truncated Sequential Neural Posterior Estimation (TSNPE) of SGM Parameter Posterior Distributions and Respective Example Synthetic EEG Spectrum (black) and SGM Simulated Spectrum (red). TSNPE with three rounds and simulation budget of 2000 simulations was used to infer SGM parameter posterior likelihoods from synthetic subjects (three examples shown in **a-c**). The left column shows three examples (a-c) of synthetic (blue) and fitted EEG spectrum (blue). Kernel density estimation (KDE) of the resulting estimated posterior probability distribution and the true value for each SGM parameter (red cross) are shown on the right column.

Figure S6: Parameter Recovery Analysis

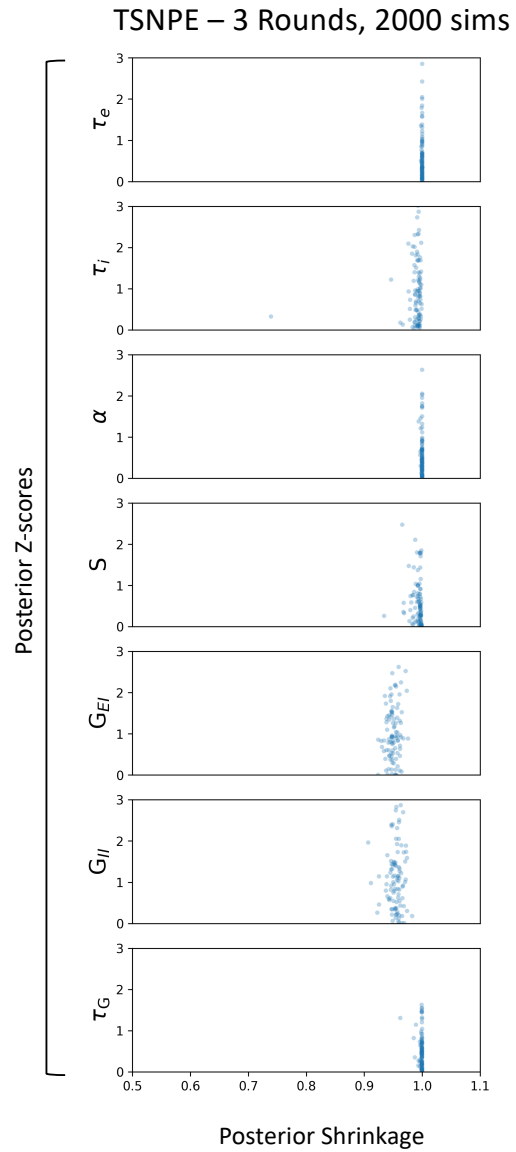
Supplementary Figure 6: SGM parameter recovery performance with SBI using 100 synthetic SGM realizations within physiologically informed prior bounds (Table 1). The predicted values versus the true values of each parameter are shown, respectively, with the gray diagonal line indicating the perfect recovery. The far left column shows parameter recovery with NRE utilizing $1E6$ simulations, the center column demonstrates NPE utilizing $1E6$ simulations, and the right column shows parameter recovery with TSNPE utilizing three rounds and 2000 simulations. α had the best R^2 across all model families, while S , G_{EI} , and τ_G had the poorest recovery error. Across all SGM parameters, NPE overall had improved mean relative estimated error (REE) compared to both TSNPE and NRE (0.0451 versus 0.0560 and 0.114, respectively).

Figure S7: Bayesian Sensitivity Analysis

Supplementary Figure 7: Bayesian sensitivity analyses can be used to identify pathology in the SBI procedure. To assess the inference's reliability with synthetic data, we analyzed the relationship between posterior z -scores and posterior shrinkage. This analysis can identify regions of poor identification, overfitting, and prior/posterior conflict[73]. z -scores were calculated as $\text{Posterior } z\text{-score} = |\mu_n(\tilde{y}) - \theta_n|/\sigma_n(\tilde{y})$ and shrinkage as $\text{Posterior Shrinkage} = 1 - \sigma_{\text{prior}}^2/\sigma_{\text{post}}^2$, following Betancourt et al.[73].

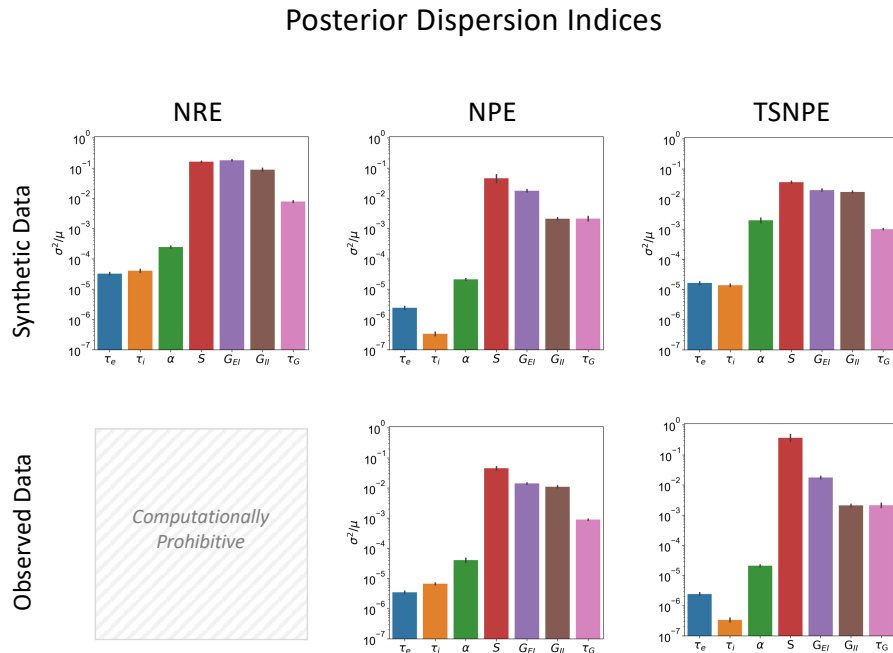
Figure S8: Bayesian Sensitivity Analysis

Supplementary Figure 8: Bayesian sensitivity analyses were used to identify pathology in the SBI procedure. We compared NPE across varying simulation budget sizes (100 to 1000000 simulations) to TSNPE at varying simulation budget sizes (100 to 2000) and varying number of rounds (two or three). Mean posterior shrinkage and z-scores from each of these models are shown for inference from 100 synthetic SGM simulations. TSNPE with three rounds and 2000 simulations overall exhibited the largest posterior shrinkage and lowest posterior z-scores. In each subplot, we plot the posterior mean of the specified simulation run. Individual z-scores and posterior shrinkages from all 100 synthetic SGM simulations for TSNPE with three rounds and 2000 simulations are demonstrated in Supplementary Figure 9.

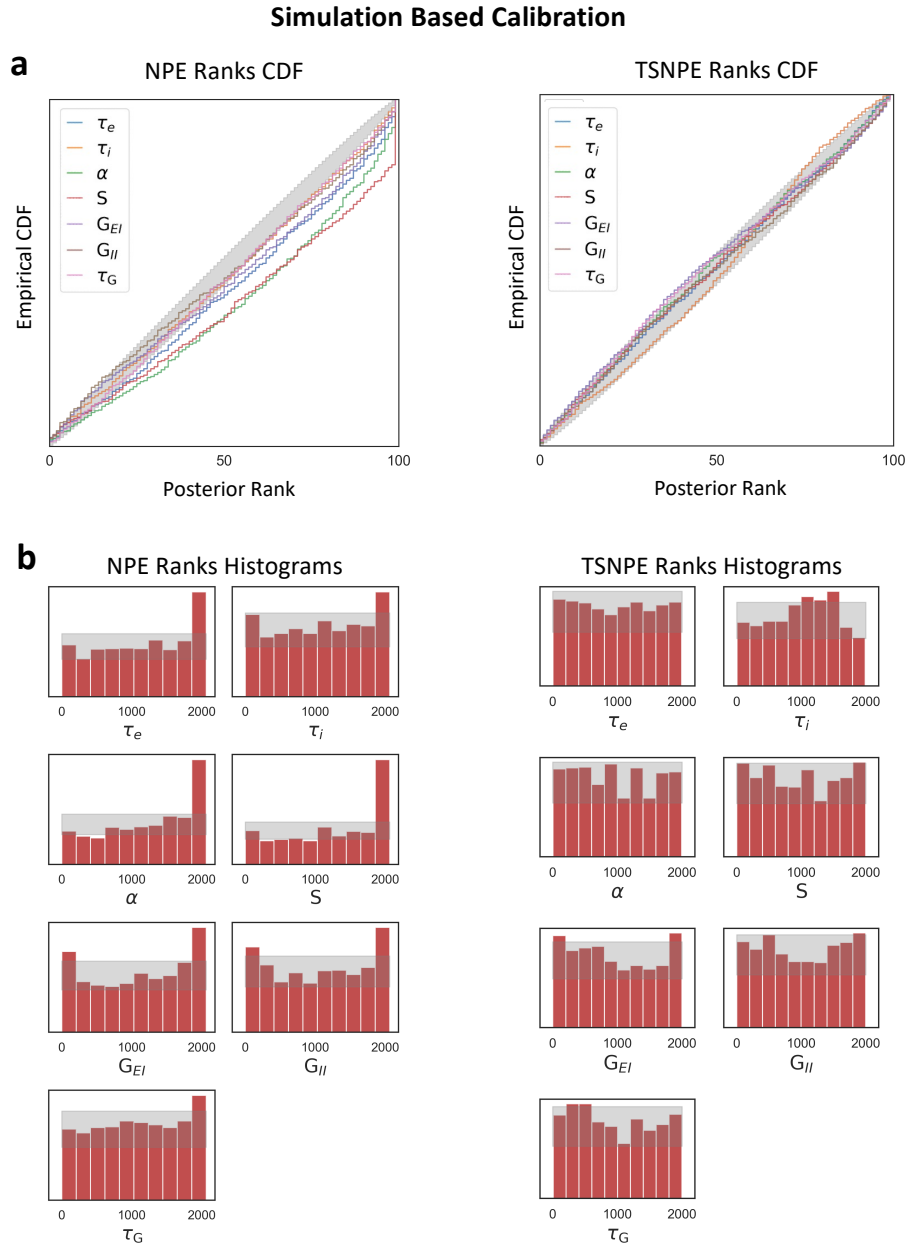
Figure S9: Bayesian Sensitivity Analysis - TSNPE with 3 rounds and 2000 simulations

Supplementary Figure 9: Posterior shrinkages and z -scores are shown for 100 synthetic simulations for each SGM parameter utilizing TSNPE with 3 rounds and 2000 simulations. There was good posterior shrinkage and posterior z -scores with good behavior for most simulations, however for each parameter there was a small tail of realizations that were overfit.

Figure S10: Posterior dispersion indices

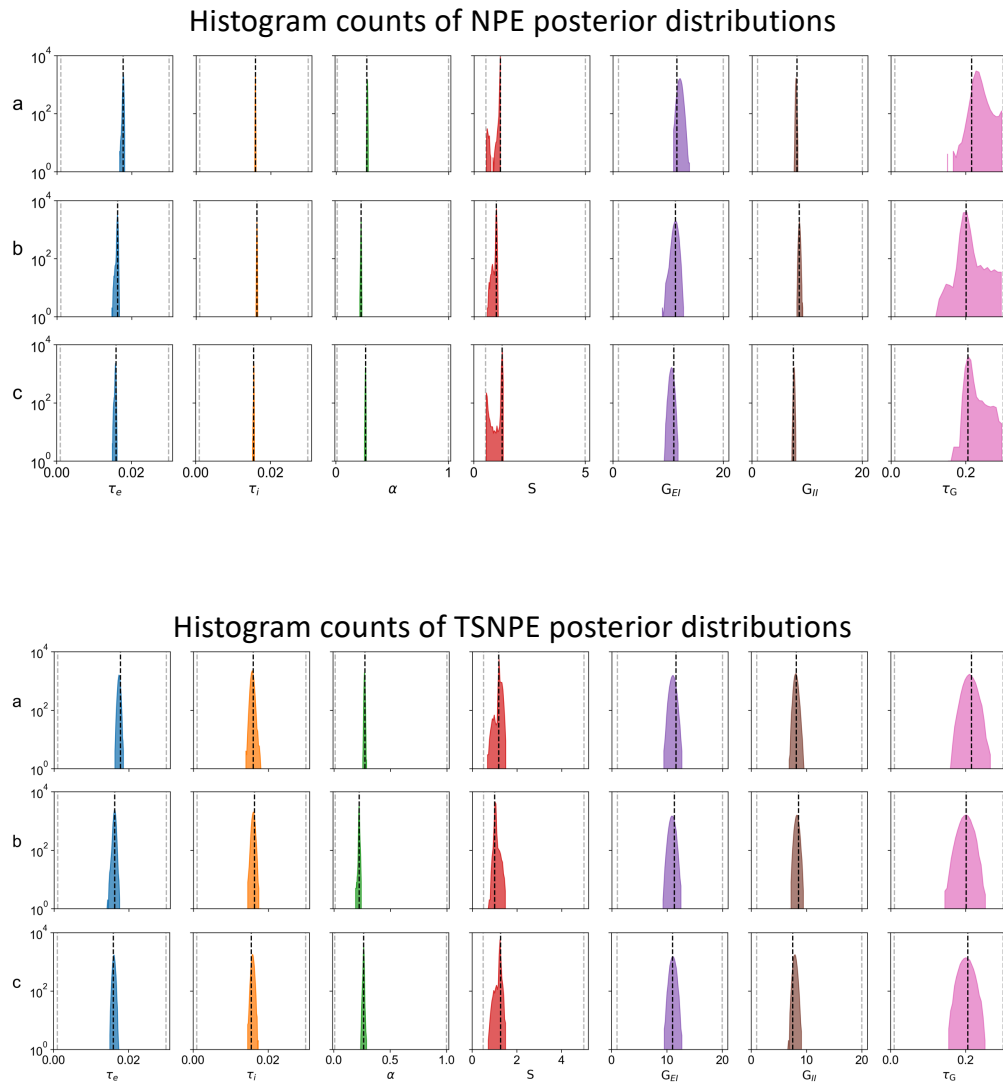


Supplementary Figure 10: Posterior dispersion indices (PDI) were obtained by normalizing variance by respective parameter mean in order to account for variation in scales across SGM parameters. NPE and TSNPE had reduced PDI relative to NRE. NPE and TSNPE had similar PDI profiles. PDI across synthetic and observed datasets revealed highest PDI in conduction speed, excitatory:inhibitory gains; aligning posterior predictive check findings that these values had relatively more degeneracy. Application of NRE on empirical data was computationally prohibitive due its utilization of MCMC sampling.

Figure S11: Simulation-based calibration

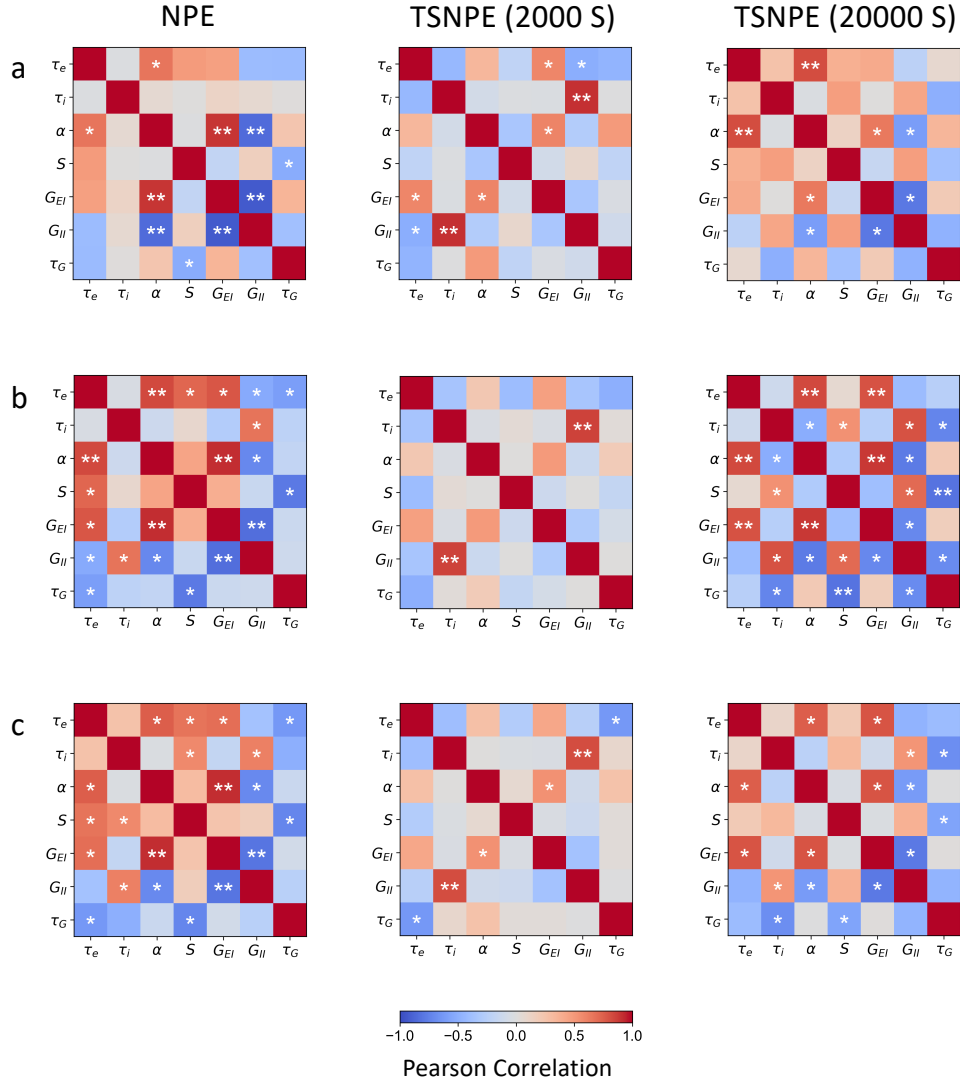
Supplementary Figure 11: a) The cumulative distribution functions (CDF) of posterior ranks are demonstrated for every parameter (colored lines), compared to the 95% confidence interval of the uniform distribution (gray diagonal region) for both NPE and TSNPE. NPE demonstrated a ranks CDF below the gray region, indicative of a non-uniform distribution, whereas TSNPE ranks CDF demonstrated lied within the gray region. b) Inspection of the ranks histograms for NPE revealed a right-skewed rank distribution indicative of systematic underestimation of the posterior mean. Inspection of the ranks histograms for TSNPE revealed relatively uniform distributed ranks across parameters; however, with subtle U-shaped distribution for τ_i and α consistent with mild under-estimation of the posterior variance.

Figure S12: Posterior Leakage



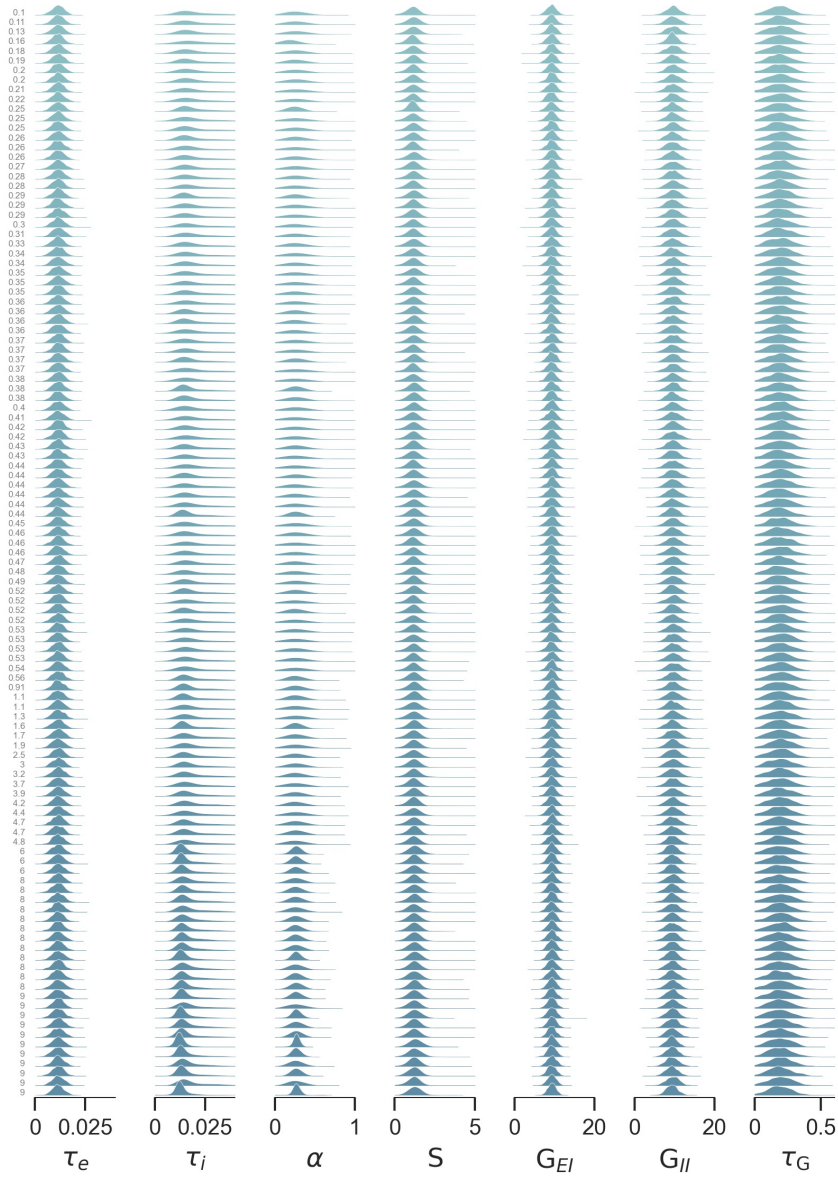
Supplementary Figure 12: Histogram counts of NPE and TSNPE estimated posterior distributions are shown, with log-scaled y-axis to identify regions containing posterior mass not readily visible in Supplementary Figures 4-6. NPE exhibited clustering of posterior mass at the prior boundary for conduction speed, indicative of posterior leakage[111]. TSNPE did not exhibit any signs of posterior leakage.

Figure S13: Posterior Distribution Pearson Correlation Matrices

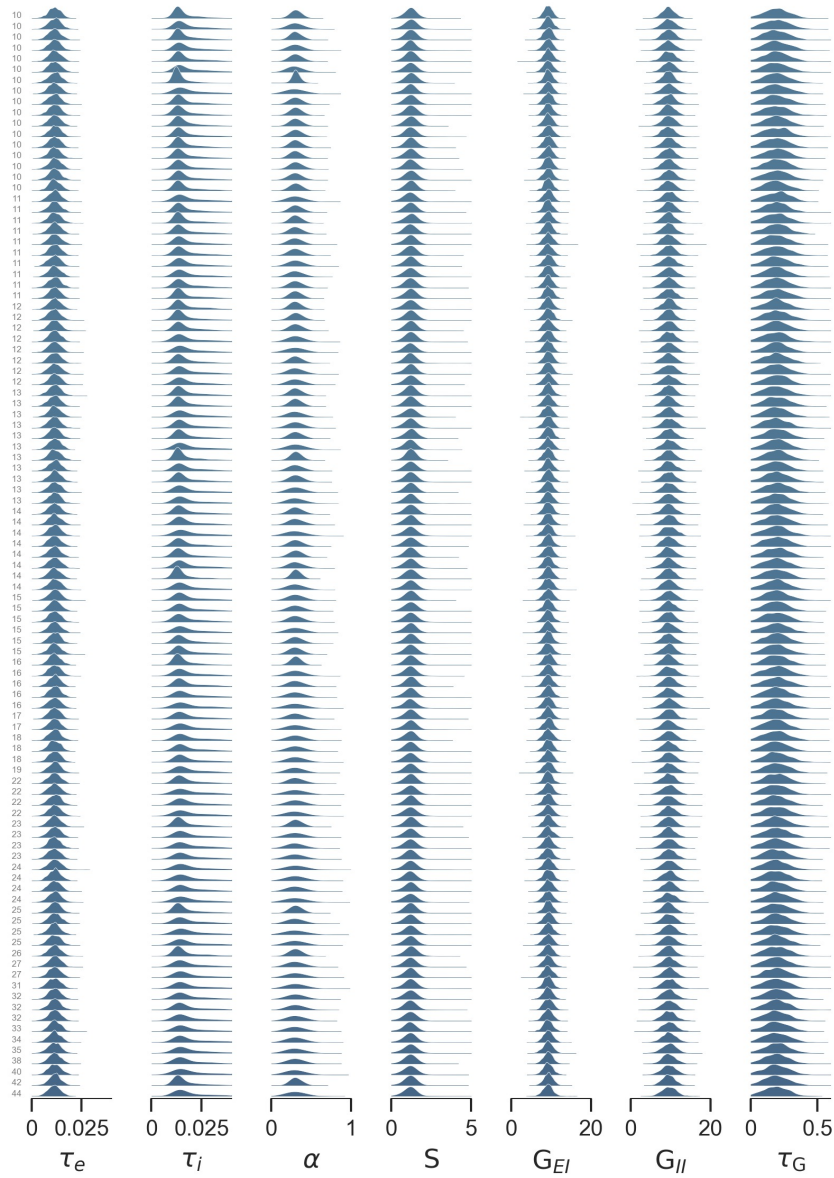


Supplementary Figure 13: We assessed for correlations in the estimated posterior joint marginal distributions utilizing Pearson correlation coefficient matrices. Rows a through c correspond with synthetic data labeled a through c in Supplementary Figures 3-5. There were significant, strong correlations ($R^2 > 0.8$) denoted by ** and significant, moderate correlations ($R^2 > 0.5$) across several joint marginals of the estimated posterior distribution. All denoted significant correlations had $p < 0.001$, adjusted for multiple comparisons using Bonferroni correction. These significant correlations are indicative of model degeneracy, wherein multiple model parameterizations yield similar spectral realizations. NPE demonstrated increased sensitivity to detect correlations between parameters when compared to TSNPE utilizing 2 rounds of sequential inference with simulation budget size of 2000. Increasing simulation budget size to 20000 simulations with TSNPE led to increased alignment in detected significant correlations with NPE. When averaging across the entire synthetic dataset, no significant correlations were observed.

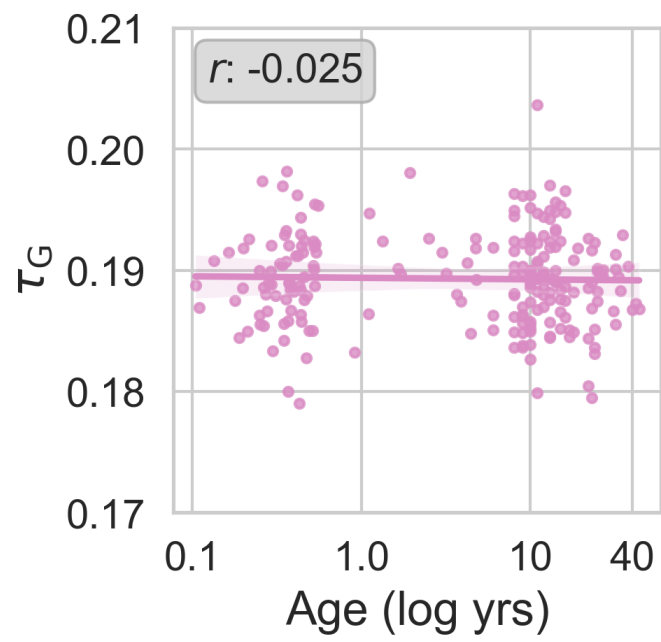
Figure S14: Posterior distribution for all subjects, part A



Supplementary Figure 14: The posterior distribution is shown for all subjects, ordered by age. The remainder of the subjects are shown in Supplementary Figure 15

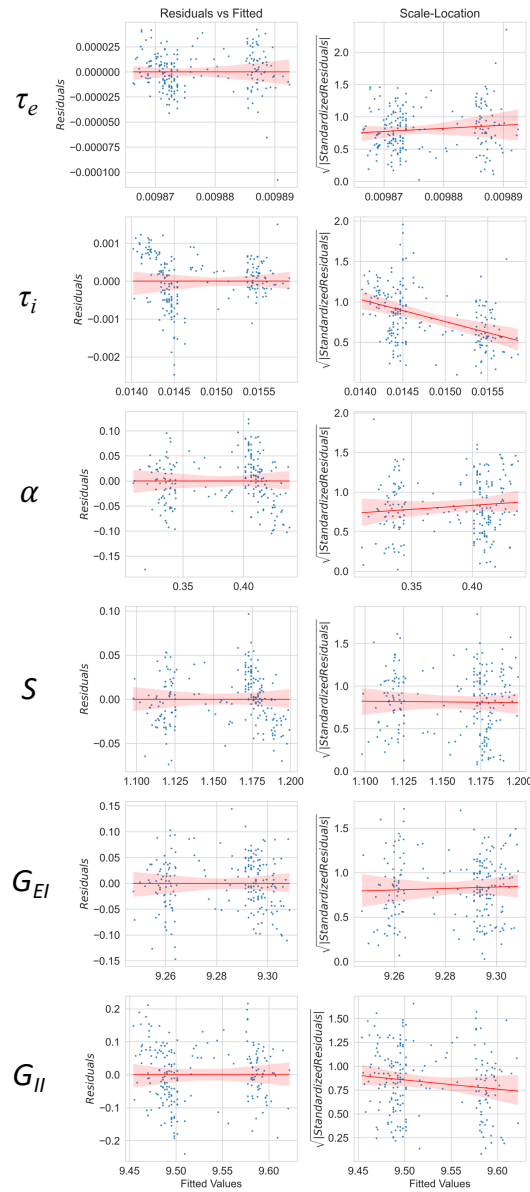
Figure S15: Posterior distribution for all subjects, part B

Supplementary Figure 15: The posterior distribution is shown for all subjects, ordered by age (continuation from Supplementary Figure 14).

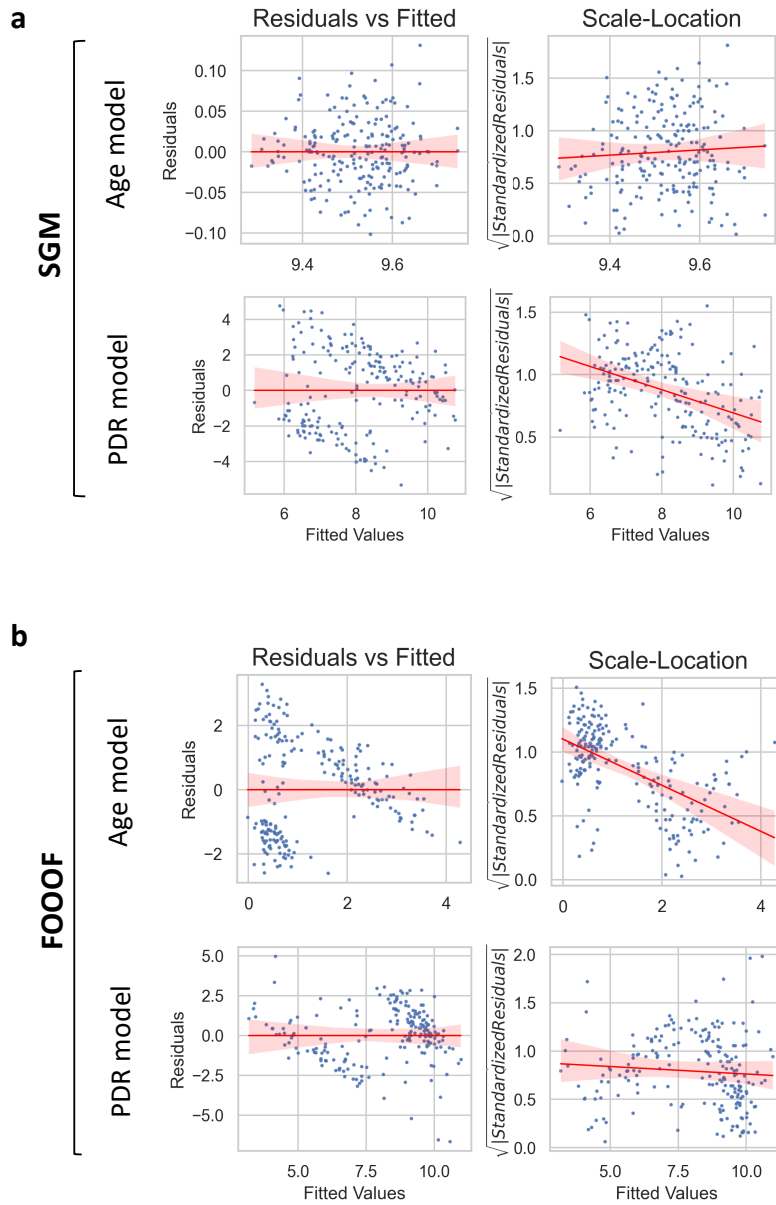
Figure S16: τ_G Relation with Age

Supplementary Figure 16: τ_G did not demonstrate time-dependent change during development.

Figure S17: Regression Diagnostics for SGM Parameter Relation with Age



Supplementary Figure 17: The left column demonstrates residuals vs. fitted values and the right column demonstrates scale-location plots across the SGM parameters found to have linear correlation with age. The red line in the residuals vs. fitted plots shows the relationship between the fitted values (predicted values) and the residuals, with the shaded regions indicating the 99.9% confidence interval. The red lines in the scale-location plots show the relationship between the fitted values (predicted values) and the square root of the absolute standardized residuals, with shaded regions indicating the 99.9% confidence intervals. Significant heteroskedasticity was found for τ_e and τ_i with BP values of 5.560 and 14.13, with p -values of 0.0179 and 0.000171.

Figure S18: Regression Diagnostics for Age Prediction Models

Supplementary Figure 18: The left column demonstrates residuals vs. fitted values and the right column demonstrates scale-location plots for the SGM and FOOOF regression models for Age and PDR prediction, respectively. The red line in the residuals vs. fitted plots shows the relationship between the fitted values (predicted values) and the residuals, with the shaded regions indicating the 99.9% confidence interval. The red lines in the scale-location plots show the relationship between the fitted values (predicted values) and the square root of the absolute standardized residuals, with shaded regions indicating the 99.9% confidence intervals. Significant heteroskedasticity was found for the SGM PDR and FOOOF Age regression models, with χ^2 of 20.52 and 57.4, respectively with p -values both less than $1e-3$.

11 Supplementary Tables

Table S1: Computation Time for TSNPE (3 rounds)

Simulation Budget	Time (min)
100	94
500	407
2000	2586